arXiv:astro-ph/9712058v1 4 Dec 1997

# Compton scattering of polarized radiation in two phase accretion disks in active galactic nuclei

CHIA-MING HSU AND OMER BLAES
Dept. of Physics, University of California, Santa Barbara, CA 93106

## ABSTRACT

We present results of radiative transfer calculations of Compton scattering of polarized radiation in a corona above an accretion disk. The corona has a plane-parallel geometry and is assumed to be homogeneous with a fixed temperature. We employ a Feautrier method to calculate the radiative transfer, incorporating the full relativistic, polarized Compton redistribution matrix. This allows us to explore a broad range of parameter space, in particular large optical depths and/or low corona temperatures, for which the iterative scattering method is very inefficient. Compared to Thomson scattering, Compton scattering generally produces smaller polarizations for featureless spectra. Distinct frequency-dependent patterns in polarization are produced near lines and edges, which can be used as diagnostics for the corona. We discuss the physics which gives rise to these results. Compton scattering can smear out Lyman edges in total flux, and at the same time produce large increases in polarization. This might help explain the steep rises in polarization observed near the Lyman limit in some quasars.

*Subject headings:* accretion, accretion disks — galaxies: active — galaxies: nuclei — polarization — radiative transfer

## 1. Introduction

Active galactic nuclei (AGN) and certain X-ray binaries are commonly believed to be powered by accretion disks. In principle, measurement of the polarization of radiation coming from these sources provides a possible test for the presence of these disks. This may be particularly true in hard X-rays where Compton scattering is generally believed to be the dominant radiation process. However, until recently, there has not been extensive discussion of Compton scattering of polarized radiation in the literature because detection of polarization in X-rays has been very difficult. With the advent of the Stellar X-Ray

Polarimeter on board Spectrum-X-Gamma, as well as other X-ray polarimetry experiments, it is becoming important to have detailed knowledge about how Compton scattering affects the polarization of X-ray radiation in accretion disk models.

This problem has also become interesting in view of the role that Compton scattering may play in smearing the Lyman edge in quasar accretion disks (Czerny & Zbyszewska 1991; Lee, Kriss, & Davidsen 1992). Such an effect might help explain why Lyman edges are generally not observed, either in absorption or emission, in quasar spectra (Antonucci, Kinney, & Ford 1989; Koratkar, Kinney, & Bohlin 1992). On the other hand, steep rises in polarization near the Lyman limit have been observed in some quasars (Impey et al. 1995, Koratkar et al. 1995). It may be that these result from scattering and absorption opacity in cool disks (Blaes & Agol 1996, but see also Shields, Wobus & Husfeld 1997). If so, then one might ask whether Compton scattering could smear the edge out in flux but preserve a rise in polarization.

It is the purpose of this paper to address these issues and to explore some of the basic physical effects of Compton scattering on polarization in the optical, ultraviolet, and X-ray portions of the spectrum. We focus primarily on the scattering from a corona above the disk, and neglect the reflection component above $\sim 10$ keV. This latter component is in fact likely to be polarized itself (Matt 1993). Similarly, we focus exclusively on the polarizing effects of the corona, and neglect reprocessing of Compton scattered radiation by the disk (cf. Matt, Fabian, & Ross 1993).

This paper is organized as follows. In section 2, we describe our radiative transfer code which fully incorporates relativistic effects on scattering (cf. Poutanen & Svensson 1996, hereafter PS96). Then we present results for idealized continuum models in section 3, followed by models with lines and edges in section 4. In section 5, we present spectra and polarization of Comptonized radiation near the Lyman limit from more realistic accretion disk atmospheres. Finally, in section 6 we summarize our conclusions. All spectra presented in this paper are local to the disk/corona system, i.e. we neglect the relativistic transfer function from the disk to the observer at infinity.

## 2. The Numerical Method

We use the simplest two-phase accretion disk model, in which the hot corona is a homogeneous, plane parallel slab of electrons and ions above a cold accretion disk (e.g. Haardt & Maraschi 1991). The only physical process we consider inside the corona is Compton scattering, and, in particular, we neglect bremsstrahlung and pair production.

Since the corona is hotter than the radiation emerging from the disk, electrons will in general lose energy to the radiation field. We assume that the cooling of the corona due to Compton scattering is immediately compensated by non-radiative heating, so that the temperature of the corona is fixed. As a result of the plane parallel geometry, the radiative transfer equation has the following one dimensional form:

$$\mu \frac{d\mathbf{I}(\tau, x, \mu)}{d\tau} = \sigma(x)\mathbf{I}(\tau, x, \mu) - \mathbf{S}(\tau, x, \mu), \tag{1}$$

where $d\tau = -\sigma_T n_e dz$ is the differential Thomson optical depth, $z$ is the vertical height measured from the base of corona, $x \equiv h\nu/m_e c^2$ is the dimensionless photon energy, $\mu = \cos\theta$, $\theta$ is the angle between the radiation propagation direction and the normal to the accretion disk plane, and $\sigma(x) \equiv \sigma_{CS}(x)/\sigma_T$ is the ratio of the thermal Compton scattering cross-section to the Thomson cross-section. The disk and corona are not expected to contain significant sources of circular polarization, and we neglect Faraday rotation completely in this paper (see, e.g. Agol, Blaes, & Ionescu-Zanetti 1997). Symmetry therefore implies that the radiation field can be polarized in only two directions: parallel to the disk plane (for which we choose the Stokes parameter $Q > 0$), or in a plane containing the radiation propagation direction and the normal to the disk plane ($Q < 0$). The polarized radiation field can be fully described by a Stokes vector $\mathbf{I}(\tau, x, \mu) \equiv \binom{I}{Q}$, from which the degree of polarization is calculated as $P = Q/I$. The source function $\mathbf{S}(\tau, x, \mu)$ has the following form (Nagirner & Poutanen 1993):

$$\mathbf{S}(\tau, x, \mu) = x^2 \int_0^\infty \frac{dx_1}{x_1^2} \int_{-1}^1 d\mu_1 \int_0^{2\pi} d\varphi_1 \int_0^{2\pi} d\varphi \hat{\mathbf{R}}(x_1, \mu_1, \varphi_1 \rightarrow x, \mu, \varphi)\mathbf{I}(\tau, x_1, \mu_1) \tag{2}$$

The radiative transfer equation can be solved by the standard Feautrier method (see, e.g., Mihalas & Mihalas 1984), with appropriate boundary conditions. Unless otherwise noted, all calculations in this paper assume no external radiation illuminating the corona from above and a perfectly absorbing accretion disk surface at the base of the corona. In addition to the radiation field emerging from the top of the corona, the radiation field scattered back to the underlying accretion disk at the base of the corona can also be solved in the same calculation. This not only provides information regarding the radiation field illuminating the accretion disk surface from the corona, but also facilitates the future possibility of coupling our results with other numerical programs for accretion disks to produce self-consistent numerical models for complete disk-corona systems. We discuss in Appendixes our discretization of the thermal source function and other numerical details.

We have tested our code by performing calculations which reproduce results published by independent authors. Figure 1 shows the degree of polarization of low frequency radiation, initially unpolarized, after Compton scattering by an extremely low temperature

optically thick corona, plotted against the classical Chandrasekhar result of polarization by Thomson scattering in an optically thick electron slab (Chandrasekhar 1960). It is clear that in the limit of low corona temperature and low frequency radiation, Compton scattering simulated by our code reduces to Thomson scattering, as expected. Also shown are calculations reproducing polarization profiles from Thomson scattering in an optically thin electron slab (Phillips & Mészáros 1986, hereafter PM86). These assume a perfectly reflecting disk surface at the corona base as the lower boundary condition, which corresponds to the transparent mid-plane condition used by PM86. The source radiation field has a $1/\mu$ intensity profile, which is similar to one of the cases considered in PM86.

In addition to these calculations in the low temperature and low frequency limit, our code also agrees with calculations of the intensity field from a large-particle Monte Carlo simulation for Compton scattering by coronae up to $\tau \approx 35$ (Magdziarz 1996, private communication).

To test the range of validity of our new code, we considered cases with extremely high Thomson depth, $\tau \geq 100$. Our code eventually fails to produce physically reasonable results for high energy radiation. This is due to inaccuracy in the calculation of the Compton redistribution matrix. In the radiative transfer equation, the thermal Compton scattering cross-section, which represents the absorption part of the scattering process, is calculated independently from the redistribution matrix in the source functions. Therefore, errors in the values of the redistribution matrix give rise to photon number imbalances in the scattering process. When the optical depth of the corona is small, errors in the final results are very small and negligible. However, when the optical depth of the corona increases, errors will accumulate. Eventually, they became so large that they render the results useless. Since the calculation of the redistribution matrix has different precision at different corona temperatures and photon energies, the maximum optical depth our code can handle varies with them. For photon energies up to 10 keV, our code provides accurate results for all corona temperatures up to 10 MeV and for scattering optical depths from 0.2 to more than 100.

We have also written a code using the iterative scattering method (PS96). Within the appropriate operating range of the iterative scattering code, the two codes produce similar results.

## 3. Physical Effects of Compton Scattering on Continuum Polarization

Although there have been some calculations of polarization resulting from Compton scattering (Haardt & Matt 1993, PS96), there has been little discussion of the differences between thermal Compton scattering and Thomson scattering. In this section, we consider some idealized problems which isolate the major physical effects.

### 3.1. Optically Thick Coronae

The polarization emerging from an optically thick, pure scattering atmosphere was calculated long ago by Chandrasekhar (1960) in the Thomson limit. The polarization is independent of frequency, because Thomson scattering is grey. This constancy with frequency remains true for an optically thick, Comptonizing corona, provided the emerging photon energies are much less than $kT_e$ and $m_e c^2$.[1] In addition, an infinite scattering depth ensures that the polarization will be independent of the input spectrum at the base of the corona. This problem therefore permits an examination of the differences between Thomson and Compton scattering in the simplest possible way.

Figure 2 shows polarization profiles of emerging radiation from optically thick coronae of various temperatures. For corona temperatures less than $10^7$ K, the results are close to the Chandrasekhar (1960) calculation based on Thomson scattering at all frequencies. Higher corona temperatures cause the degree of polarization to drop for all viewing angles, but it continues to be independent of frequency. Although the emerging intensity is smaller for higher corona temperatures due to upscattering of photons out of the plotted range, it is uniform over frequency and has an angular distribution which is indistinguishable from the Chandrasekhar (1960) limb darkening law. This suggests that the high temperature polarization drop arises purely from changes in the scattering cross-section.

Consider a Cartesian coordinate system in which a monoenergetic beam of energy $x_1$ propagates in the positive $x$-direction. Suppose the beam is one hundred percent linearly polarized along the $z$-axis. Then if this beam interacts with thermal electrons, the differential cross-section for the total scattered intensity at energy $x$ is given from equation (2) by

$$\frac{1}{\sigma_T}\frac{d\sigma_I}{d\Omega} = \frac{x^2}{x_1^2}(\hat{R}_{11} + \hat{R}_{12}), \tag{3}$$

[1]The reason is that there is then no energy scale in the scattering, and the polarization, like the intensity $I_\nu \propto \nu^3$, must be a power law. However, the only power law which is bound between -1 and 1 is a constant.

and that for the Stokes parameter $Q$ at energy $x$ is

$$\frac{1}{\sigma_T}\frac{d\sigma_Q}{d\Omega} = \frac{x^2}{x_1^2}(\hat{R}_{21} + \hat{R}_{22}). \tag{4}$$

Figure 3 depicts these angular distributions of scattered radiation for thermal Compton scattering by electrons at a temperature of 1 keV. The beam pattern depicted is for both incident and scattered photons with the same energy of 0.1 keV. Note that outgoing radiation is 100% polarized, as expected for Thomson scattering. This case is in fact well within the Thomson limit, but the results exhibit significantly more forward scattering than the classical dipole pattern. This is a consequence of our choice of equal energy for incident and scattered photons. The Thomson limit of equation (3) is

$$\frac{1}{\sigma_T}\frac{d\sigma_I}{d\Omega}(\mu,\phi,x) = \frac{3}{16\pi x_1}\frac{1-\mu^2}{[\pi\Theta(1-\cos\tilde{\theta})]^{1/2}}\exp\left[-\frac{(x-x_1)^2}{4x_1^2(1-\cos\tilde{\theta})\Theta}\right], \tag{5}$$

where $\tilde{\theta}$ is the scattering angle [$\cos\tilde{\theta} = (1-\mu^2)^{1/2}\cos\phi$], and $\Theta \equiv kT_e/(m_ec^2)$. When integrated over all scattered energies $x$, this reduces to the usual dipole formula for Thomson scattering.

Figures 4 and 5 depict the beam patterns for corona temperatures of 100 keV and 10 MeV, respectively. It is clear that as the corona temperature increases, the redistribution profiles become more symmetric around the propagation direction of incident radiation (the forward direction), and the polarized intensity becomes smaller compared to the total intensity. This is due to the fact that the isotropic electron velocity distribution of the corona randomizes the direction and polarization of scattered radiation around the forward direction through relativistic aberration.

This explains the decrease of polarization from the Chandrasekhar level for high temperature optically thick coronae. Since the scattering cross-section of linearly polarized incident radiation becomes more symmetric around the forward direction, then if the incident radiation is unpolarized, the chance of photons scattering in a given direction from two perpendicular polarization states in the incident beam is very similar. Furthermore, scattered radiation from purely linearly polarized incident radiation is no longer 100% polarized, as can be seen in figure 4 and 5. This also helps reduce the polarization in the resulting spectrum.

The above behavior of the Compton scattering cross-section should be expected in all phenomena related to a low energy radiation field (tested up to 0.3 keV in our case) which is scattered by a high temperature electron cloud. This is not to be confused with the fact that the Klein-Nishina cross-section for ultra-relativistic photons in the electron

rest frame becomes unpolarized for large scattering angles (see, e.g., Berestetskii, Lifshitz, & Pitaevskii 1982). Although the two effects are similar in that both of them reduce polarization of scattered radiation, one is due to the relativistic effects of ultra-high energy incident photons, whereas the other is due to large random motions of thermal electrons. The reduction of polarization by the thermal motion of electrons is less severe when the incident photon energy is large, since then the random motions of the electrons become small compared to the incident photon momentum.

### 3.2. Continuum Polarization from Optically Thin Coronae

Figure 6 shows polarization profiles of emerging radiation from coronae at fixed temperature with various scattering optical depths. The polarization increases with increasing optical depth. Since the input spectrum at the base of the corona is unpolarized, the thicker the corona, the larger the polarization because of increased electron scattering. Note that these results are different from PM86 (cf. Fig. 1) due to different boundary conditions and a different input spectrum at the base of the corona. Here we use a perfectly absorbing accretion disk surface with a uniform, isotropic spectrum as the input. In PM86, they use a transparent mid-plane (reflective boundary) condition with $1/\mu$ intensity profile sources along the corona midplane. Their source angular distribution and the reflected radiation enhance the anisotropy of angular distribution of the radiation field, resulting in a higher magnitude of polarization for optically thin coronae.

Knowing the effects of Compton scattering on low energy radiation, we now turn our attention to higher photon energies. The behavior of Compton scattering can be seen most clearly with unpolarized, monochromatic incident light. In order to see the effects of progressively higher order scattering, we show results calculated by the iterative scattering method. Figure 7(a) shows the Comptonized spectrum emerging from a $\tau = 0.5$, $kT_e = 100$ keV corona which is being irradiated from below by an isotropic distribution of soft (5 eV) unpolarized monoenergetic photons. Two viewing angles are shown, and the lowest scattering orders are also depicted. As is well known, the high energy part of the spectrum is a power law with a thermal cutoff above the electron temperature. Since incident light is monochromatic, all radiation away from the source frequency is scattered radiation from the corona itself. For a moderately optically thin corona, as shown here, effective lines of sight, from which scattered radiation can be accumulated, are longest in the horizontal direction. The emerging spectrum is therefore limb brightened (except at the source frequency, see below.)

Figure 7(b) shows the corresponding degree of polarization. As first noted by Haardt

& Matt (1993), the polarization is initially positive near the monochromatic source energy, where single scattering dominates the spectrum, but then becomes negative at higher energies where the second and higher order scatterings dominate. For the first scattering order, the incident radiation is the attenuated, unscattered source from the base of the corona. This radiation is limb darkened because the optical depth to the base of the corona increases for more horizontal lines of sight. It is this limb darkening which produces the resulting positive polarization near the source energy. Higher scattering orders produce negatively polarized radiation from limb brightened, scattered radiation (cf. Fig. 7(a)). This flip in polarization between the first and second scattering orders is a strong diagnostic. This could be used to confirm whether or not an observed anisotropy break in intensity is really due to the change in scattering order, although the anisotropy break itself is most easily detectable for near face-on viewing angles (Haardt 1993) where the polarization is weakest.

Figure 8 shows the intensity and polarization emerging from a $\tau = 0.5$, $kT_e = 100$ keV corona with an isotropic, unpolarized, quasi-monoenergetic ($E_{photon} \approx 5$ eV) source at the base of the corona. Four different viewing angles are shown. The polarization of high energy scattered radiation varies from $-4.5\%$ to $-16.5\%$, with an edge-on view having the largest degree of polarization. Figure 9 shows the intensity and polarization emerging at a viewing angle of $\mu = 0.069$ (edge-on view) from $\tau = 0.5$ coronae with the same source at the corona base. This time the corona temperature is different. For a factor of ten decrease of corona temperature from $kT_e = 100$ keV to $kT_e = 10$ keV, the magnitude of the degree of polarization of high energy scattered radiation increases dramatically from 16.5% to 45%. Figure 10 shows the intensity and polarization emerging at a viewing angle of $\mu = 0.069$ (edge-on view) from $kT_e = 100$ keV coronae with the same source at the corona base. Three different scattering optical depths are shown, and the degree of polarization of high energy scattered radiation varies from $-10\%$ of $\tau = 1.0$ to $-20\%$ of $\tau = 0.3$. For the three parameters, edge-on views combined with small corona temperatures and small scattering optical depths produce the largest degree of polarization in a plane normal to the accretion disk surface (negative). This can be understood from our previous discussion. Since thin coronae have very anisotropic angular distributions of scattered radiation, they produce larger degrees of polarization for edge-on views compared with thicker coronae. And the small corona temperature reduces the de-polarization effect of the thermal motion of the electrons.

## 4. Comptonization of Lines and Edges

### 4.1. Polarization Signature of Lines by Compton Scattering

Figure 11 shows the intensity and polarization emerging from a $\tau = 0.5$, $kT_e = 100$ keV corona with an isotropic, unpolarized, continuum background and an emission line feature illuminating the base of the corona. The overall intensity is smaller for an edge-on view because the edge-on view has a longer line of sight, thus more photons are upscattered out of the plotted range. Note that for a moderately thin corona of $\tau = 0.5$ with the continuum input shown here, the main component in the emerging spectrum is the unscattered source. However, scattering broadens the emission line and shifts it toward higher energies. For the low energy continuum below the emission line in the original input spectrum, the emerging polarization exhibits the behavior discussed in Section 3.1. The degree of polarization is independent of frequency, and has the same value as if the input spectrum were completely uniform. At the energy range of the emission line, the degree of polarization rises. At energies higher than the emission line, the degree of polarization drops below the level before the onset of the emission line, then rises again to approach the level before the onset of the emission line from below.

The transfer equation is linear in the radiation field, and all this behavior can therefore be explained by Compton scattering on the continuum background and emission line separately. For a frequency independent continuum source, Compton scattering produces degrees of polarization which are independent of frequency well below photon energies $\sim \min[kT_e, m_e c^2]$. For an emission line, like the quasi-monoenergetic source in Section 3.2, Compton scattering produces positive polarization at energies around the line and negative polarization away from the line. When we put both together, we have the result in figure 11. Away from the emission line, especially the low energy part, the degree of polarization is largely determined by Compton scattering effects on the uniform continuum background. Near the emission line, the degree of polarization exhibits a rise when the emission line alone would have a positive polarization and a drop when the emission line alone would have a negative polarization.

If there is an absorption line instead of an emission line in an otherwise uniform continuum background, the results are the reverse of the emission line spectrum (figure 12). As before, the overall intensity is smaller for edge-on views. Again, Compton scattering broadens the absorption line and shifts it toward higher energies. Instead of a rise then a drop in the degree of polarization toward the high energy end of the spectrum, the absorption line causes a larger drop first at the energy of the absorption line, then a rise at higher energies. As we discussed in section 3.2, the first scattering order from a monoenergetic source has positive polarization, while higher scattering orders have negative polarization. The emerging polarization for a uniform continuum is actually a

balance between those two opposite polarizations when all scattering orders, including the attenuated, unscattered source, are mixed together in the final emerging radiation. Inside the absorption line, there is less unscattered radiation in the original input spectrum at the base of the corona. This makes the corresponding unscattered and first order scattered radiation, which have zero and positive polarization, respectively, less important when mixed with higher order scattered radiation from outside the line. The result is a drop in the emerging degree of polarization inside the absorption line due to the larger negative polarization. Similarly, at energies higher than the absorption line, there is a lack of higher order scattered radiation originating from inside the absorption line. Therefore, a rise in the degree of polarization is seen there due to the smaller effect of negative polarization.

The rise and fall in the degree of polarization of lines with respect to the continuum level after Compton scattering is a generic phenomenon in plane parallel geometry. The magnitude of the rise and fall in polarization for a line is affected by the strength of the line. Figure 13 shows the intensity and polarization emerging along $\mu = 0.069$ (edge-on view) from a $\tau = 0.5$, $kT_e = 100$ keV corona with an isotropic, unpolarized, continuum background plus emission lines of varying strength as the input spectrum at the base of the corona. Not surprisingly, stronger lines have larger rises and drops in polarization, while the polarization of the continuum stays the same, indepedent of line strength. Note that the high corona temperature in this case keeps the polarization small in all cases.

### 4.2. Polarization of Edges by Compton Scattering

The effects of Compton scattering on emission and absorption edges are quite different. In the context of the two phase accretion disk, where the corona is hot, Compton scattering of disk radiation by electrons in the corona tends to increase photon energy. Hence absorption edges have more photons scattered into the low intensity region, which has higher energy, than emission edges. The polarization signatures are different, too. Emission edges show more complex structure than absorption edges, again due to the asymmetry of photon energy drift.

Figure 14 shows the intensity and polarization emerging from a $\tau = 0.5$, $kT_e = 100$ keV corona with an isotropic, unpolarized absorption edge spectrum illuminating at the base of the corona. The intensity is assumed to be uniform both above and below the edge. Photons scattered into the high energy, originally low intensity region form a power law spectrum, as expected from Compton scattering in general. Since the scattered radiation dominates this part of the emerging spectrum, the polarization exhibits large negative values here, akin to the high energy spectrum of a Comptonized, monochromatic input

spectrum discussed in Section 3.2. The upturn in polarization for photon energies larger than 1 keV is due to the fact that high order scattered radiation from frequencies lower than the discontinuity is becoming weaker compared to radiation from frequencies higher than the discontinuity. For frequencies lower than the discontinuity, the polarization is independent of frequency and has the same value it would have had if the input spectrum were completely uniform.

Figure 15 shows the same thing for an emission edge. There is still a power law spectrum produced on the low energy side near the discontinuity, but the slope is much steeper than the one in the absorption edge case. This is because the power law in the emission edge case is formed by downscattered photons from the high energy side of the discontinuity, and downscattered radiation has an intrinsically steeper slope than upscattered radiation. The more complex structure of the polarization in the emission edge case can be understood by considering the two sides of the discontinuity separately. On the low energy side, the emerging radiation is dominated by downscattered radiation from the high energy side, as can be seen from the intensity plot. Hence the resulting polarization is similar to that of the low energy downscattered region of a monochromatic input source discussed in Section 3.2 (cf. Figs. 7-10). The polarization is positive right next to the discontinuity, and turns negative at lower energies. At even lower energy, downscattered radiation from the high energy side becomes less important, and both the intensity and degree of polarization return to their frequency-independent values for a uniform spectrum as discussed above. On the high energy side of the discontinuity, the polarization rises and then drops back toward the level for a uniform input spectrum. This is similar to the behavior on the high energy side of the Comptonized absorption line discussed above (cf. Fig. 12), and arises for exactly the same reasons.

Just as in the case of lines, the variation in polarization across the edge depends on the edge height. Figure 16 shows the intensity and polarization emerging along $\mu = 0.069$ (edge-on view) from a $\tau = 0.5$, $kT_e = 100$ keV corona with an isotropic, unpolarized absorption edge spectrum with various edge heights illuminating the base of the corona. As expected, larger edge heights cause larger dips into negative polarization, while the polarization away from the edge is independent of the edge height.

## 5. The Lyman Edge

Many accretion disk models of AGN predict a strong Lyman edge feature in the spectrum, while only a very small number of observed AGN spectra possess Lyman edge features, and even these are weak at best. Czerny and Zbyszewska (1991) pointed out

that Compton scattering of disk radiation by a corona can smear out the Lyman edge. We confirm this suggestion by calculating spectra after Compton scattering from an accretion disk atmosphere, which has a strong Lyman edge feature (Agol 1997, private communication). For simplicity, we assume the corona to have uniform optical depth and temperature over the disk.

Figure 17 and 18 show the intensity and polarization entering to and emerging from a $\tau = 0.5$, $kT_e = 100$ keV corona, with viewing angle of $\mu = 0.211$ and $\mu = 0.789$, respectively. From the intensity plots, it is clear that the sizes of the Lyman and Balmer edges are both reduced by Compton scattering, and photons are shifted toward higher energies. The Lyman and Balmer edges are almost smeared out by Compton scattering in the more edge-on view in figure 17. However, intensity discontinuities are still evident in the more face-on view of figure 18, although they have been reduced.

The changes in polarization caused by Compton scattering are more subtle. An edge-on view changes the degree of polarization more so that most of the polarization features disappear. For example, in figure 17, the polarization discontinuities at the Lyman and Balmer edges before Compton scattering are almost smeared out, and the steep rise in polarization blueward of the Lyman edge has completely disappeared. Figure 18 shows that a more face-on view better preserves both polarization discontinuities and the rise of polarization blueward of the Lyman edge, even though the edges in total intensity are reduced. This can be attributed to the fact that for a corona with $\tau = 0.5$, a more edge-on view has a longer effective line of sight, and so the effect of Compton scattering is greater. Calculations with different corona scattering optical depths show that larger scattering optical depths produce results similar to the more edge-on view shown here. Smaller optical depths have results similar to the more face-on view, retaining more of the original features in the disk atmosphere spectrum, both in intensity and degree of polarization. If steep rises in polarization blueward of the Lyman edge in several quasars as observed via HST are actually produced in the accretion disk atmospheres (Blaes & Agol 1996), then this calculation implies that we should be looking at optically thin corona with a more face-on view, if the corona exists at all.

The detailed behavior of the polarization can be understood from our results in Sections 3 and 4. In figure 17, the polarization for radiation frequencies lower than the Lyman edge increases as a result of Compton scattering. For radiation frequencies far above the Lyman edge, the original disk atmosphere spectrum has extremely small intensity. Therefore, higher order Compton scattered radiation, which has a large negative degree of polarization, dominates this part of emerging spectrum.

A major criticism against Compton scattering as a means of getting rid of Lyman

edges in AGN spectra is that the radiation should then have substantial polarization (Antonucci 1992), at least if Compton scattering imparted a polarization comparable to that of Thomson scattering. We have shown in section 3 that in general Compton scattering produces smaller polarizations than Thomson scattering for a featureless continuum. Nevertheless, our calculations here show that at the corona temperatures expected in AGN ($< 100$ keV), if Compton scattering succeeds in smearing an edge, it does indeed generally produce a subtantial polarization in the optical/UV portion of the spectrum. Hence if Compton scattering is present, some means must be invoked to reduce the polarization to observed values, such as Faraday rotation (e.g. Agol & Blaes 1996).

Shields, Wobus, and Husfeld (1997) recently demonstrated that taking into account the relativistic transfer from the black hole to a distant observer, accretion disk atmosphere models have difficulty explaining the steep rise in polarization blueward of the Lyman edge observed in PG 1222+228 and PG 1630+377. They further showed that a good fit to the observed spectropolarimetry data can be achieved by assuming an ad hoc disk spectrum with a sharp Lyman edge in absorption in total flux together with a sharp jump in polarization towards high frequencies at the Lyman edge. Compton scattering can produce just such a spectrum. In fact, it can even produce a steep rise in polarization *without* a jump in total intensity. In Section 4.2, we showed that an absorption edge spectrum has large (negative) polarization blueward of the edge after Compton scattering, if the input spectrum at the base of the corona is unpolarized (figure 14). With appropriate corona parameters, Compton scattering can easily produce polarizations as high as 45% in a plane containing the radiation propagation direction and the normal to the disk plane. This is a promising alternative for explaining the steep rise of polarization blueward of Lyman edge observed in AGNs.

## 6. Conclusions

We have presented calculations of Compton scattering of polarized radiation in accretion disk coronae using a finite difference Feautrier method. Our calculations can be improved by incorporating other sources of radiation, such as bremsstrahlung, or absorption terms. There are also existing techniques to use the same one dimensional radiative transfer equation on calculations of more complex corona geometry (PS96), making our code useful for cases other than plane parallel coronae. By calculating the radiation reflected by the corona back to the disk atmosphere, our code can be coupled to a code that calculates the emerging spectrum from the accretion disk atmosphere. Iteration between the two codes can then produce a fully self-consistent spectrum.

By considering a number of idealized input spectra at the base of the corona, we have identified some generic features of the effect of inverse Compton scattering on polarization. Starting with unpolarized, monoenergetic radiation at the base of the corona, the emerging polarization is positive near the frequency of the unscattered source and negative further away. When the input spectrum has uniform intensity over a range of frequencies, radiation from different source frequencies with different orders of scattering is mixed together to produce the emerging spectrum, with a frequency independent degree of polarization which is determined by the viewing angle, corona temperature, and corona scattering depth. If there are intensity variations in the input spectrum such as lines or edges, there will be corresponding generic frequency-dependent patterns in the polarization, which depend on the strength and profile of the lines or edges.

As first suggested by Czerny and Zbyszewska (1991), Compton scattering can be successful in smearing out the Lyman edge, provided the optical depth along the line of sight is sufficiently high. Generally this also smears out any polarization features arising from the underlying disk atmosphere. However, there are regions of parameter space where such features are preserved even though the Lyman edge intensity jump is markedly reduced (cf. Fig. 18). When Compton scattering is successful in smearing out an edge, it generally imparts a significant polarization to the overall spectrum. This may have to be removed by Faraday rotation, for example, in order not to conflict with the generally low optical polarizations observed in type 1 AGN. Finally, Compton scattering can produce very large, negative polarizations in regions of the spectrum where the disk itself produces very little radiation. In this way a steep rise in polarization can be produced near the Lyman limit, even though the resulting Comptonized intensity is smeared out and exhibits very little jump.

We thank E. Agol, I. Hubeny, P. Magdziarz, and A. Zdziarski for useful conversations. This work was supported by NSF grant AST 95-29230.

## A. Source Functions in Finite Difference Form

The original radiative transfer equation, as described in Section 2, is

$$\mu \frac{d\mathbf{I}(\tau, x, \mu)}{d\tau} = \sigma(x)\mathbf{I}(\tau, x, \mu) - \mathbf{S}(\tau, x, \mu), \tag{A1}$$

where

$$\mathbf{S}(\tau, x, \mu) = x^2 \int_0^\infty \frac{dx_1}{x_1^2} \int_{-1}^{1} d\mu_1 \tilde{\mathbf{R}}(x, \mu; x_1, \mu_1)\mathbf{I}(\tau, x_1, \mu_1) \tag{A2}$$

and

$$\tilde{\mathbf{R}}(x,\mu;x_1,\mu_1)=\int_0^{2\pi}d\varphi_1\int_0^{2\pi}d\varphi\hat{\mathbf{R}}(x_1,\mu_1,\varphi_1\rightarrow x,\mu,\varphi). \tag{A3}$$

We define $\mathbf{j}$ and $\mathbf{h}$ in the usual way:

$$\mathbf{j}(\tau,x,\mu)=\frac{1}{2}[\mathbf{I}(\tau,x,\mu)+\mathbf{I}(\tau,x,-\mu)], \tag{A4}$$

and

$$\mathbf{h}(\tau,x,\mu)=\frac{1}{2}[\mathbf{I}(\tau,x,\mu)-\mathbf{I}(\tau,x,-\mu)], \tag{A5}$$

where $\mu$ is restricted to $1\geq\mu\geq 0$ hereafter.

Then, the radiative transfer equation can be written as

$$\mu\,\frac{d\mathbf{h}(\tau,x,\mu)}{d\tau}=\mathbf{j}(\tau,x,\mu)-\mathbf{S}^{+}(\tau,x,\mu) \tag{A6}$$

and

$$\mu\,\frac{d\mathbf{j}(\tau,x,\mu)}{d\tau}=\mathbf{h}(\tau,x,\mu)-\mathbf{S}^{-}(\tau,x,\mu), \tag{A7}$$

where

$$\mathbf{S}^{\pm}(\tau,x,\mu)=\frac{1}{2}[\mathbf{S}(\tau,x,\mu)\pm\mathbf{S}(\tau,x,-\mu)]. \tag{A8}$$

Note that compared to many other forms of scattering, Compton scattering is unusual in that the source function is not invariant under the transformation $\mu\rightarrow-\mu$. Hence there is a source function term on the right hand side of equation (A7). The source functions, written in terms of Compton redistribution matrixes, are

$$\mathbf{S}^{+}(\tau,x,\mu)=x^2\int_0^{\infty}\frac{dx_1}{x_1^2}\int_0^{1}d\mu_1[\tilde{\mathbf{R}}(x,\mu;x_1,\mu_1)+\tilde{\mathbf{R}}(x,\mu;x_1,-\mu_1)]\mathbf{j}(\tau,x_1,\mu_1) \tag{A9}$$

$$\mathbf{S}^{-}(\tau,x,\mu)=x^2\int_0^{\infty}\frac{dx_1}{x_1^2}\int_0^{1}d\mu_1[\tilde{\mathbf{R}}(x,\mu;x_1,\mu_1)-\tilde{\mathbf{R}}(x,\mu;x_1,-\mu_1)]\mathbf{h}(\tau,x_1,\mu_1) \tag{A10}$$

In deriving this, we have used one of the symmetry properties of the redistribution matrix:

$$\tilde{\mathbf{R}}(x,\mu;x_1,\mu_1)=\tilde{\mathbf{R}}(x,-\mu;x_1,-\mu_1) \tag{A11}$$

which comes from the fact that scattering processes do not depend on the choice of coordinate orientation.

Now we have to discretize the above integrals for the source functions. We assume that the intensities $\mathbf{j}(\tau)$ and $\mathbf{h}(\tau)$ at a certain depth do not change dramatically within an angle-frequency cell for a chosen finite difference grid, so that we can approximate them as constant within each cell. Further improvement, if necessary, can be introduced by using

cubic spline functions to represent the intensity $\mathbf{j}(\tau)$ and $\mathbf{h}(\tau)$ (Adams, Hummer, & Rybicki 1971).

Based on our assumption, we can then write the source functions as

$$\mathbf{S}_k^+(\tau) = \sum_{k'=1}^{K} \mathbf{R}_{k,k'}^j \mathbf{j}_{k'}(\tau) \tag{A12}$$

and

$$\mathbf{S}_k^-(\tau) = \sum_{k'=1}^{K} \mathbf{R}_{k,k'}^h \mathbf{h}_{k'}(\tau), \tag{A13}$$

where

$$\mathbf{R}_{k,k'}^j = x_k^2 \int_{x_{1,k'l}}^{x_{1,k'h}} \frac{dx_1}{x_1^2} w_\mu(\mu_{1k'}) [\tilde{\mathbf{R}}(x_k, \mu_k; x_1, \mu_{1k'}) + \tilde{\mathbf{R}}(x_k, \mu_k; x_1, -\mu_{1k'})], \tag{A14}$$

$$\mathbf{R}_{k,k'}^h = x_k^2 \int_{x_{1,k'l}}^{x_{1,k'h}} \frac{dx_1}{x_1^2} w_\mu(\mu_{1k'}) [\tilde{\mathbf{R}}(x_k, \mu_k; x_1, \mu_{1k'}) - \tilde{\mathbf{R}}(x_k, \mu_k; x_1, -\mu_{1k'})], \tag{A15}$$

$w_\mu(\mu_{1k'})$ is the integration weight associated with the angular abscissas $\mu_{1k'}$ of the $k'$ angle-frequency cell, and $[x_{1,k'l}, x_{1,k'h}]$ is the frequency range of the $k'$ angle-frequency cell. Note that we have arranged all angle-frequency cells into a long vector using only one index.

The radiative transfer equations then become

$$\mu \frac{d\mathbf{h}_k(\tau)}{d\tau} = \mathbf{j}_k(\tau) - \sum_{k'=1}^{K} \mathbf{R}_{k,k'}^j \mathbf{j}_{k'}(\tau) \tag{A16}$$

and

$$\mu \frac{d\mathbf{j}_k(\tau)}{d\tau} = \mathbf{h}_k(\tau) - \sum_{k'=1}^{K} \mathbf{R}_{k,k'}^h \mathbf{h}_{k'}(\tau), \tag{A17}$$

and we can proceed to a discretized optical depth mesh as usual in the Feautrier method.

## B. Frequency Weights in Redistribution Matrix for Low Corona Temperature

When the corona temperature is low, the redistribution matrix for Compton scattering is sharply peaked in frequency since the energy shift of photons per scattering is small. For sufficiently low corona temperatures, the frequency finite difference grid cannot resolve the large but narrow variation in the redistribution matrix. In order to correctly calculate the frequency weights when the redistribution matrix is narrowly peaked, without using a large number of frequency points which would be wasteful when the redistribution matrix is smooth, we need a versatile integration scheme.

We have devised such a scheme which works as follows. For any frequency range $[x_A, x_B]$, we evaluate the redistribution matrix $\tilde{\mathbf{R}}$ at the midpoint $x_C$ and two end points $x_A, x_B$. Then we take the ratio of the 11 components of the matrix between the midpoint and whichever end point which has the larger value. For example, if $\tilde{\mathbf{R}}_{11}(x_A) < \tilde{\mathbf{R}}_{11}(x_B)$, then the ratio $r = \tilde{\mathbf{R}}_{11}(x_C)/\tilde{\mathbf{R}}_{11}(x_B)$. If the ratio $r$ is smaller than a chosen critical value (we use $10^{-5}$ or $10^{-7}$), we flag it as a large variation in the redistribution matrix. The routine will then perform the integration over the smaller value range ($[x_A, x_C]$ in the above example) using the trapezoidal rule, and recursively call itself to integrate over the larger value range ($[x_C, x_B]$ in the above example). Otherwise, if the ratio $r$ is larger than the critical value, the routine will calculate the whole range using a Gauss-Legendre quadrature (we use 40 points).

### C. Thermally Averaged Compton Scattering Cross-Section

To calculate the thermally averaged Compton scattering cross-section $\sigma(x) \equiv \sigma_{CS}(x)/\sigma_T$, we use the full integral expression in PS96. However, that expression fails numerically for low corona temperatures $\Theta \equiv kT_e/(m_e c^2)$ and low photon energies $x$. For low $\Theta$, the modified Bessel function $K_2(1/\Theta)$ used in the normalization underflows, while for low $x$, the integrand cannot be calculated accurately due to high order cancellation of the $2/x$ term. We therefore switch to various asymptotic expressions for low $\Theta$ or low $x$ as needed.

For corona temperatures below $10^7$ K, we use

$$\sigma(x) = 1 - 2x + \frac{26}{5}x^2 \qquad x \leq 10^{-3} \tag{C1}$$

and

$$\sigma(x) = \frac{3}{8x^2}\left[4 + \left(x - 2 - \frac{2}{x}\right)\ln(1+2x) + \frac{2x^2(1+x)}{(1+2x)^2}\right] \qquad x > 10^{-3}, \tag{C2}$$

which are accurate to 1 part in $10^7$ in the ranges indicated.

For corona temperatures above $10^7$ K, we use

$$\sigma(x) = \frac{1}{K_2(1/\Theta)}\sum_{n=0}^{\infty}(-2x)^n a_n K_{n+2}(1/\Theta), \tag{C3}$$

where

$$a_n = \frac{3}{8}\left(n + 2 + \frac{2}{n+1} + \frac{8}{n+2} - \frac{16}{n+3}\right), \tag{C4}$$

for $x \leq x_c$, where

$$x_c = 8.865351 \times 10^{-4}(1/\Theta)^{0.353736486}. \tag{C5}$$

Otherwise, for $x > x_c$, we use the full integral expression of PS96.

Using 8 terms in the modified Bessel function series and 40-point Gauss-Laguerre quadrature for the full integral expression, the error in $\sigma(x)$ is less than 1 part in $10^6$ for corona temperatures above $10^7$ K.

## REFERENCES

Adams, T. L., Hummer, D. G., & Rybicki, G. B. 1971, JQSRT, 11, 1365

Agol, E. 1997, private communication

Agol, E., & Blaes, O. 1996, MNRAS, 282, 965

Agol, E., Blaes, O., & Ionescu-Zanetti, C. 1997, MNRAS, in press

Antonucci, R. R. J., Kinney, A. L., & Ford, H. C. 1989, ApJ, 342, 64

Antonucci, R. 1992, in Testing the AGN Paradigm, ed. S. Holt, S. Neff, & C. M. Urry (New York: AIP), 486

Berestetskii, V. B., Lifshitz, E. M., & Pitaevskii, L. P. 1982, Quantum Electrodynamics (Oxford:Pergamon)

Blaes, O., & Agol, E. 1996, ApJ, 469, L41

Chandrasekhar, S. 1960, Radiative Transfer (New York:Dover)

Czerny, B., & Zbyszewska, M. 1991, MNRAS, 249, 634.

Haardt, F. 1993, ApJ, 413, 680

Haardt, F., & Maraschi, L. 1991, ApJ, 380, L51.

Haardt, F., & Matt, G. 1993, MNRAS, 261, 346

Impey, C. D., Malkan, M. A., Webb, W. & Petry, C. E. 1995, ApJ, 440, 80

Koratkar, A., Antonucci, R. R. J., Goodrich, R. W., Bushouse, H., & Kinney, A. L. 1995, ApJ, 450, 501

Koratkar, A. P., Kinney, A. L., & Bohlin, R. C. 1992, ApJ, 400, 435

Lee, G., Kriss, G. A., & Davidsen, A. F. 1992 in Testing the AGN Paradigm, ed. S. Holt, S. Neff, & C. M. Urry (New York:AIP), 159

Magdziarz, P. 1996, private communication

Matt, G. 1993, MNRAS, 260, 663

Matt, G., Fabian, A. C., & Ross, R. R. 1993, MNRAS, 264, 839

Mihalas, D., & Mihalas, B.W. 1984, Foundations of Radiation Hydrodynamics, (New York:Oxford University Press)

Nagirner, D.I., & Poutanen, J. 1993, A&A, 275, 325

Phillips, K.C., & Mészáros, P. 1986, ApJ, 310, 284

Poutanen, J., & Svensson, R. 1996, ApJ, 470, 249

Shields, G. A., Wobus, L., & Husfeld, D. 1997, ApJ, submitted.

This preprint was prepared with the AAS LaTeX macros v4.0.

Fig. 1.— Degree of polarization of radiation emerging from an extremely low temperature corona with $T_e = 1.16$ K. The input spectrum is a uniform, unpolarized, low energy radiation field extending up to $E = 0.332$ keV. Open squares are from a $\tau = 10.0$ corona with a perfectly absorbing accretion disk surface and isotropic sources at the corona base. Other points are for a perfectly reflecting disk surface at the corona base and a source having a $1/\mu$ intensity profile. Crosses, filled squares, open triangles, and filled triangles are from coronae of $\tau = 10.0$, 2.0, 1.0, and 0.20, respectively. The solid line is the classical Chandrasekhar (1960) result of polarization by Thomson scattering in an optically thick electron slab.

Fig. 2.— Degree of polarization of radiation emerging from $\tau = 10.0$ coronae with various temperatures. The input spectrum is a uniform, isotropic, unpolarized, low energy radiation field extending up to $E = 0.332$ keV, and the polarization profiles shown are calculated for the same energy range. Open squares, filled squares, filled triangles, open triangles, crosses are from coronae with $kT_e = 1$, 10, 100, $10^3$, and $10^4$ keV, respectively. The solid line is the classical Chandrasekhar result of polarization by Thomson scattering in an optically thick electron slab.

Fig. 3.— Cross-sections of the scattered intensity profile for $kT_e = 1$ keV, purely linearly polarized incident radiation of 0.1 keV, and no change in the photon energy upon scattering. The solid line is the surface of total intensity (polarized and unpolarized), and the dotted line is the surface of polarized intensity, which has the same polarization direction as the incident radiation. Here, the dotted line lies on top of the solid line.

Fig. 4.— Same as Fig. 3, except $kT_e = 100$ keV and the incident and final photon energies are 10 keV.

Fig. 5.— Same as Fig. 3, except $kT_e = 10$ MeV and the incident and final photon energies are 1 MeV.

Fig. 6.— Degree of polarization of radiation emerging from $kT_e = 10$ keV coronae with various scattering optical depth. The input spectrum is a uniform, isotropic, unpolarized, low energy radiation field extending up to $E = 0.332$ keV, and the polarization profiles shown are calculated for the same energy range. Filled squares, filled triangles, open triangles, crosses are from coronae with $\tau = 10.0$, 1.0, 0.5, and 0.2, respectively. Note that filled squares are the same as the filled squares in figure 2.

Fig. 7.— (a) Specific intensity and (b) degree of polarization ($Q_x/I_x$) emerging from a $\tau = 0.5$, $\Theta = 0.20$ corona with an isotropic, unpolarized, monoenergetic ($x = 10^{-5}$) input spectrum. The solid and dashed curves correspond to $\mu = 0.211$ and 0.789 viewing angles, respectively. The heavy curves represent the total emerging spectrum, while the numbered

pairs correspond to the lowest scattering orders.

Fig. 8.— Specific intensity and degree of polarization emerging from a $\tau = 0.5$, $kT_e = 100$ keV corona with an isotropic, unpolarized, quasi-monoenergetic ($E_{photon} \approx 5$ eV) input spectrum. Open squares (dotted line), filled squares (solid line), open triangles (short dashed line), filled triangles (long dashed line) correspond to $\mu = 0.069$, 0.330, 0.670, and 0.931 lines of sight, respectively.

Fig. 9.— Specific intensity and degree of polarization emerging along a line of sight with $\mu = 0.069$ (i.e. edge-on view) from $\tau = 0.5$ coronae with an isotropic, unpolarized, quasi-monoenergetic ($E_{photon} \approx 5$ eV) input spectrum. Filled squares (solid line) and open squares (dotted line) correspond to coronae with electron temperatures of $kT_e = 10$ and 100 keV, respectively.

Fig. 10.— Specific intensity and degree of polarization emerging along $\mu = 0.069$ from $kT_e = 100$ keV coronae with an isotropic, unpolarized, quasi-monoenergetic ($E_{photon} \approx 5$ eV) input spectrum. Filled triangles (dashed line), open squares (dotted line), and filled squares (solid line) correspond to coronae with scattering optical depths of $\tau = 1.0$, 0.5, and 0.3, respectively.

Fig. 11.— Specific intensity and degree of polarization emerging from a $\tau = 0.5$, $kT_e = 100$ keV corona with an isotropic, unpolarized, continuum background plus an emission line as the input spectrum at the base of the corona. Open squares (dotted line), filled squares (short dashed line), open triangles (long dashed line), filled triangles (dot-dashed line) correspond to $\mu = 0.069$, 0.330, 0.670, and 0.931 lines of sight, respectively. The solid line in the intensity plot is the input spectrum at the base of the corona. The polarization of the input spectrum is zero everywhere.

Fig. 12.— Same as Fig. 11 but for an absorption line.

Fig. 13.— Specific intensity and degree of polarization emerging at a viewing angle of $\mu = 0.069$ from a $\tau = 0.5$, $kT_e = 100$ keV corona with an isotropic, unpolarized, continuum background plus various emission lines as the input spectrum at the base of the corona. Open squares (dotted line) are the same as the open squares in figure 10. Open triangles (dashed line) and filled squares (solid line) have an original emission line two and four times as strong as the open squares, respectively.

Fig. 14.— Specific intensity and degree of polarization emerging from a $\tau = 0.5$, $kT_e = 100$ keV corona with an isotropic, unpolarized absorption edge spectrum as the input spectrum at the base of the corona. Open squares (dotted line), filled squares (short dashed line),

open triangles (long dashed line), filled triangles (dot-dashed line) correspond to $\mu = 0.069$, 0.330, 0.670, and 0.931 viewing angles, respectively. The solid line in the intensity plot is the input spectrum at the base of the corona. The polarization of the input spectrum is zero everywhere.

Fig. 15.— Same as Fig. 14 but for an emission edge as the input spectrum.

Fig. 16.— Specific intensity and degree of polarization emerging at a viewing angle of $\mu = 0.069$ (edge-on view) from a $\tau = 0.5$, $kT_e = 100$ keV corona with an isotropic, unpolarized absorption edge spectrum as the input spectrum at the base of the corona. Open squares (dotted line) are the same as the open squares in figure 13, for which the intensity ratio across the discontinuity is 1:1000. Open triangles (short dashed line) and filled squares (long dashed line) have intensity ratios of 1:100 and 1:10, respectively. The solid lines in the intensity plot are the input spectra at the base of the corona for all three cases.

Fig. 17.— Specific intensity and degree of polarization entering at the base of the corona and emerging at the top of the corona at a viewing angle of $\mu = 0.211$ from a $\tau = 0.5$, $kT_e = 100$ keV corona. Open squares (dotted line) are the spectrum at the base of the corona, which is produced by an accretion disk atmosphere calculation by Agol. Filled squares (solid line) are the spectrum emerging at the top of the corona after Compton scattering.

Fig. 18.— Same as Fig. 17 but for a viewing angle of $\mu = 0.789$.

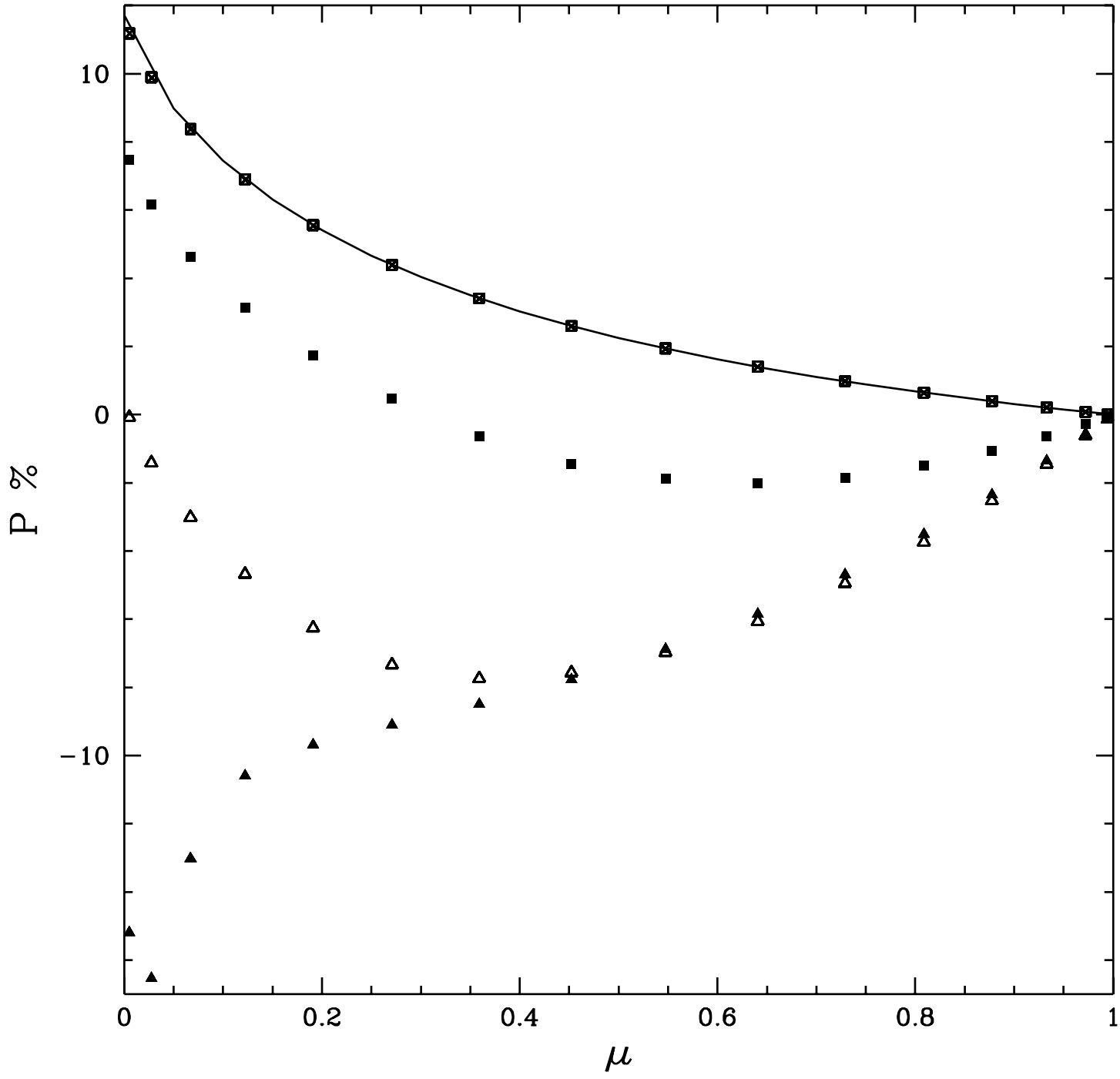
10
0
−10
P %
0
0.2
0.4
0.6
0.8
1
μ

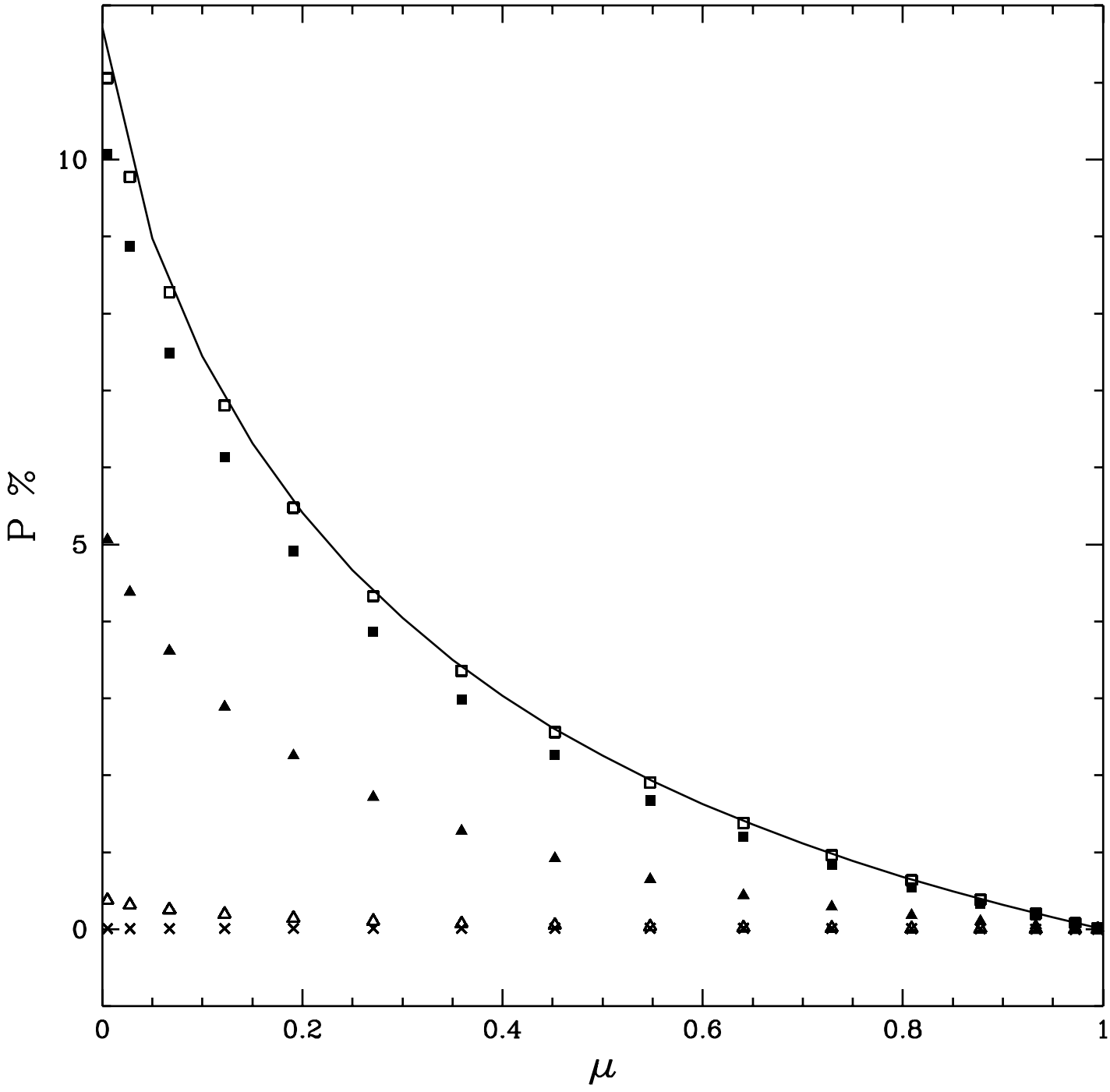
10
5
0
P %
0
0.2
0.4
0.6
0.8
1
μ

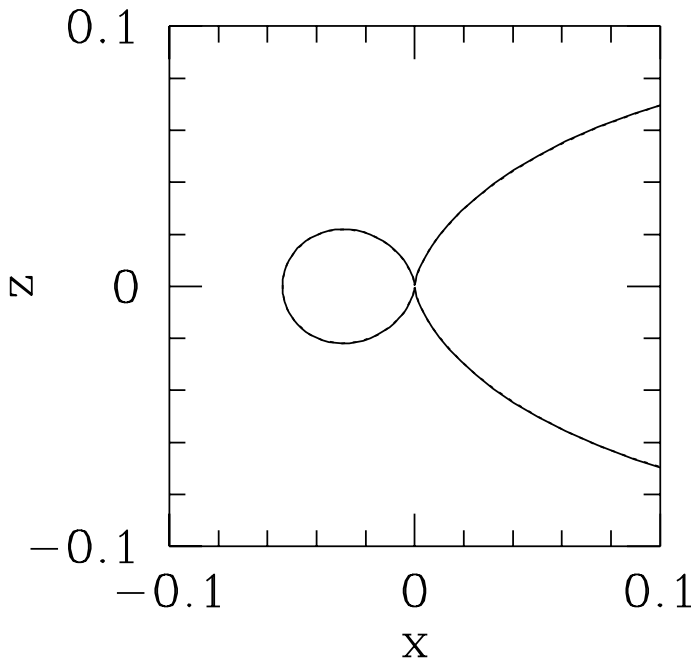
0.1
0
−0.1
z
−0.1
0
0.1
x

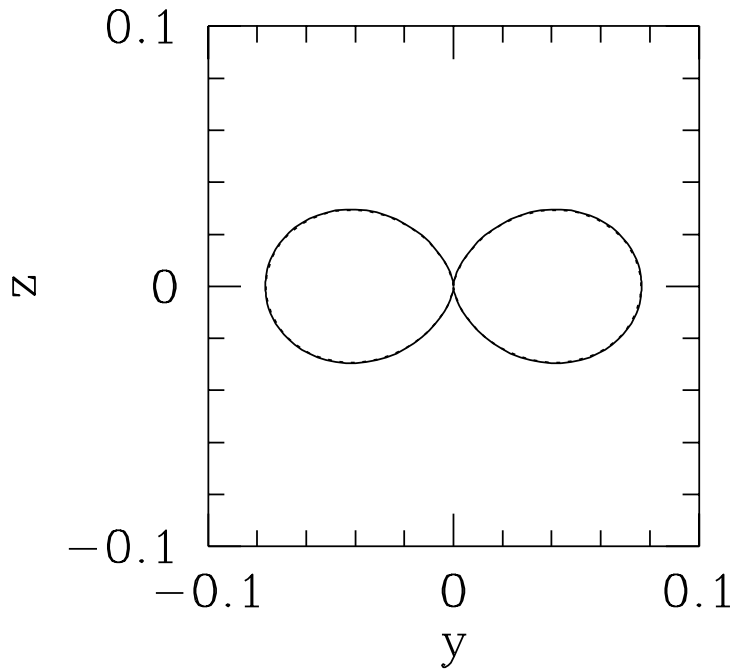
0.1
0
−0.1
z
−0.1
0
0.1
y

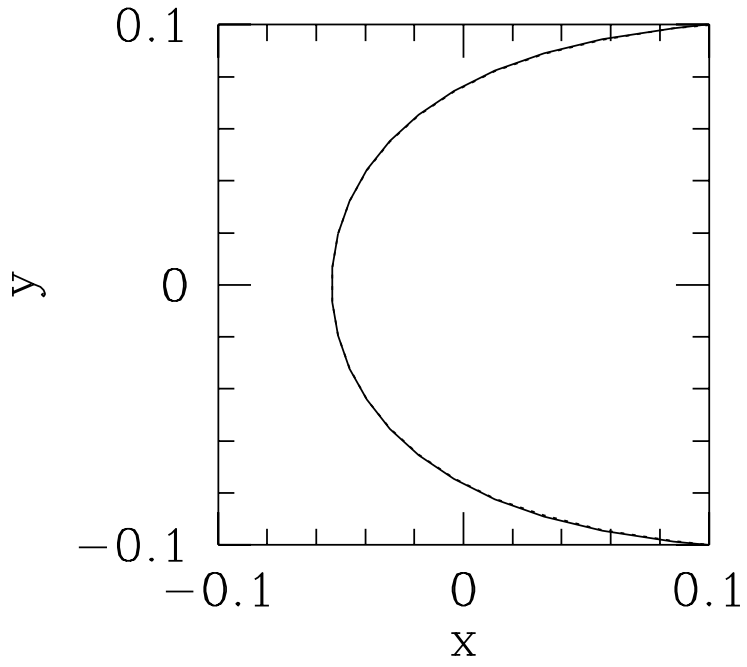
0.1
0
−0.1
y
−0.1
0
0.1
x

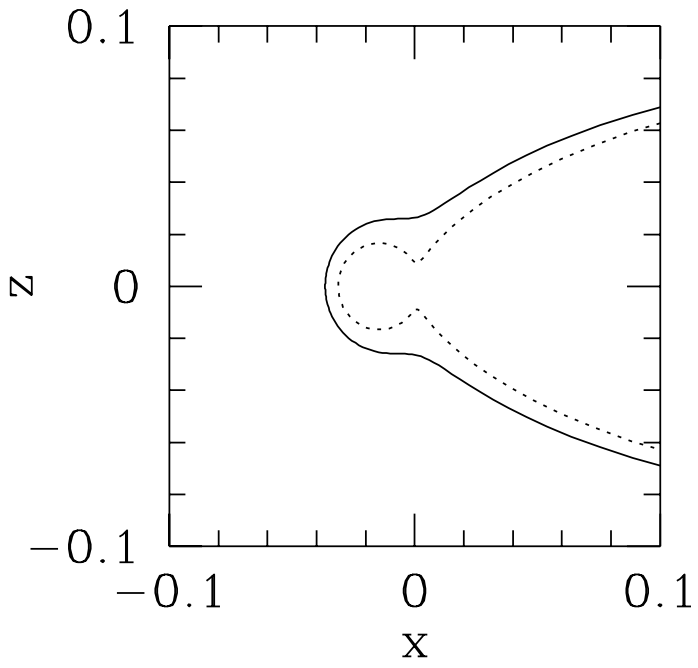
0.1
0
−0.1
z
−0.1
0
0.1
x

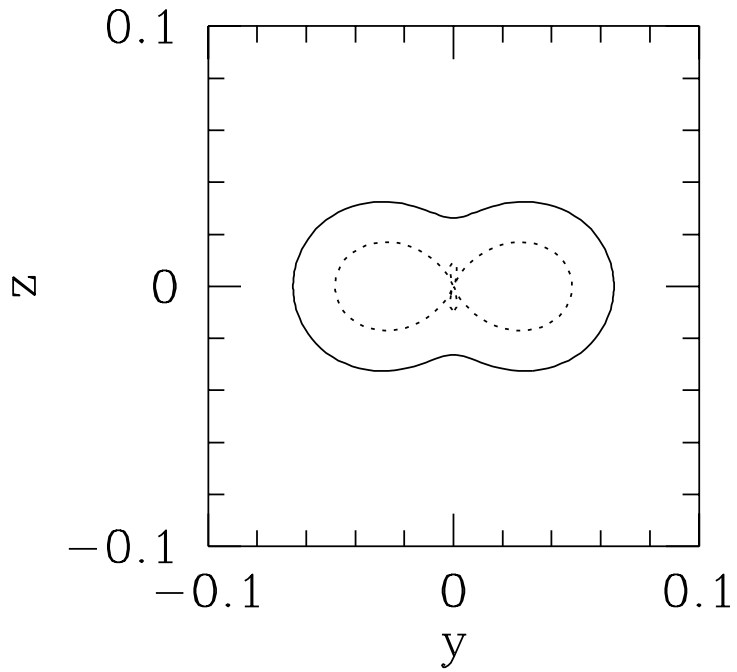
0.1
0
−0.1
z
−0.1
0
0.1
y

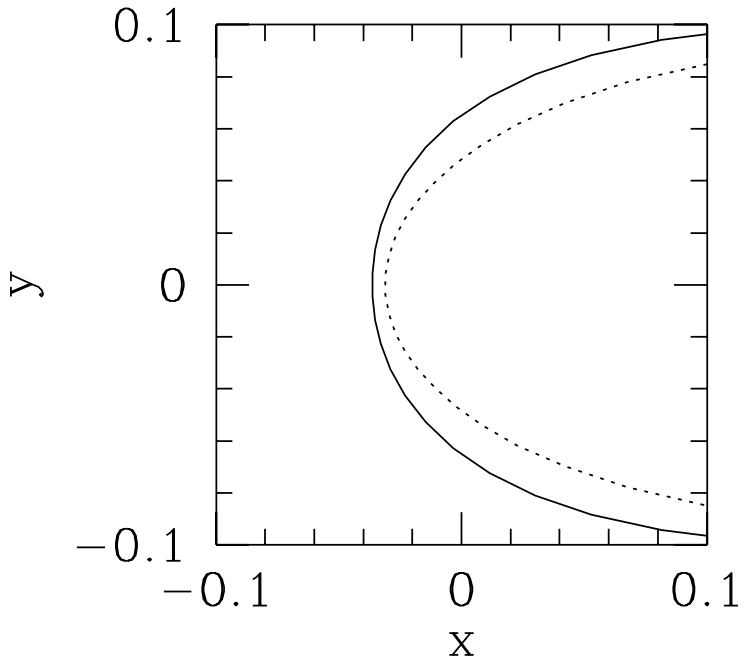
0.1
0
−0.1
y
−0.1
0
0.1
x

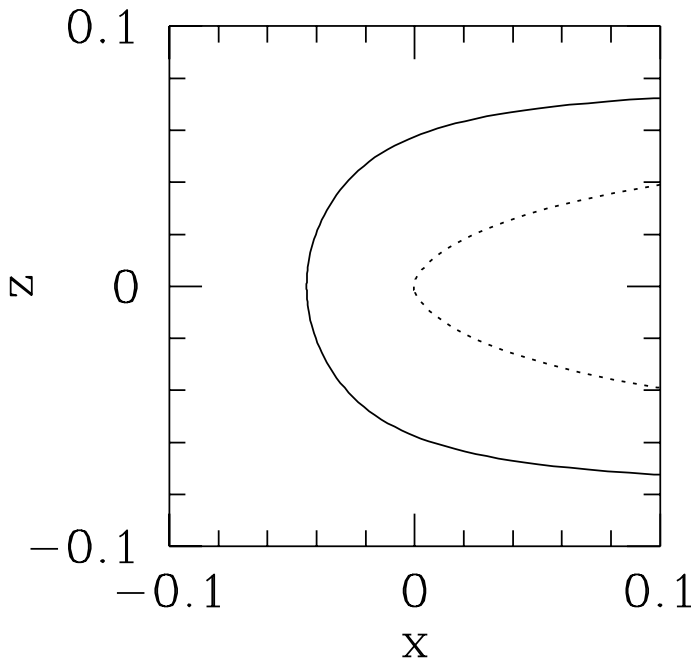
0.1
0
−0.1
z
−0.1
0
0.1
x

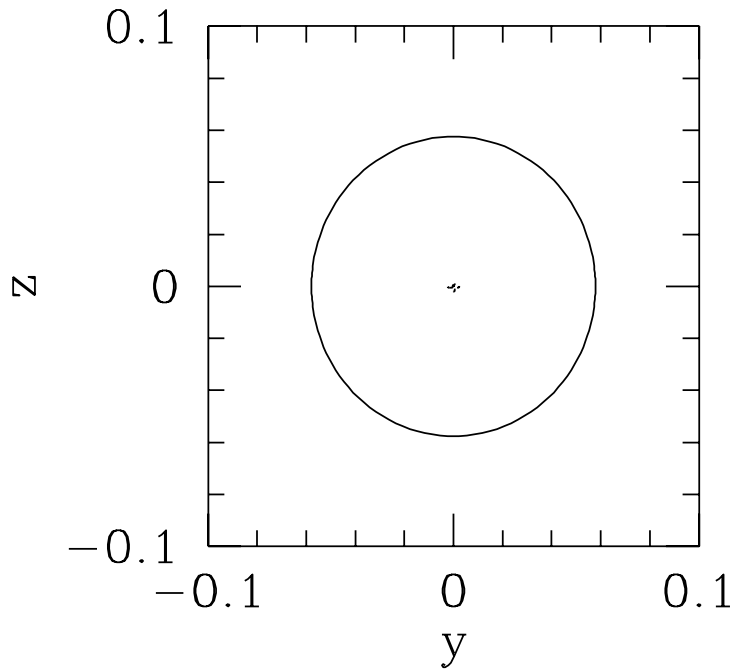
0.1
0
−0.1
z
−0.1
0
0.1
y

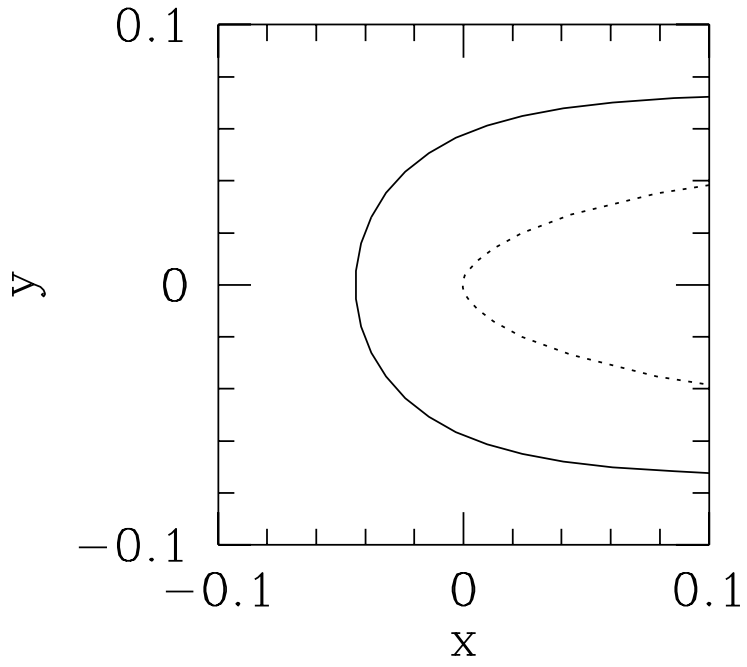
0.1
0
−0.1
y
−0.1
0
0.1
x

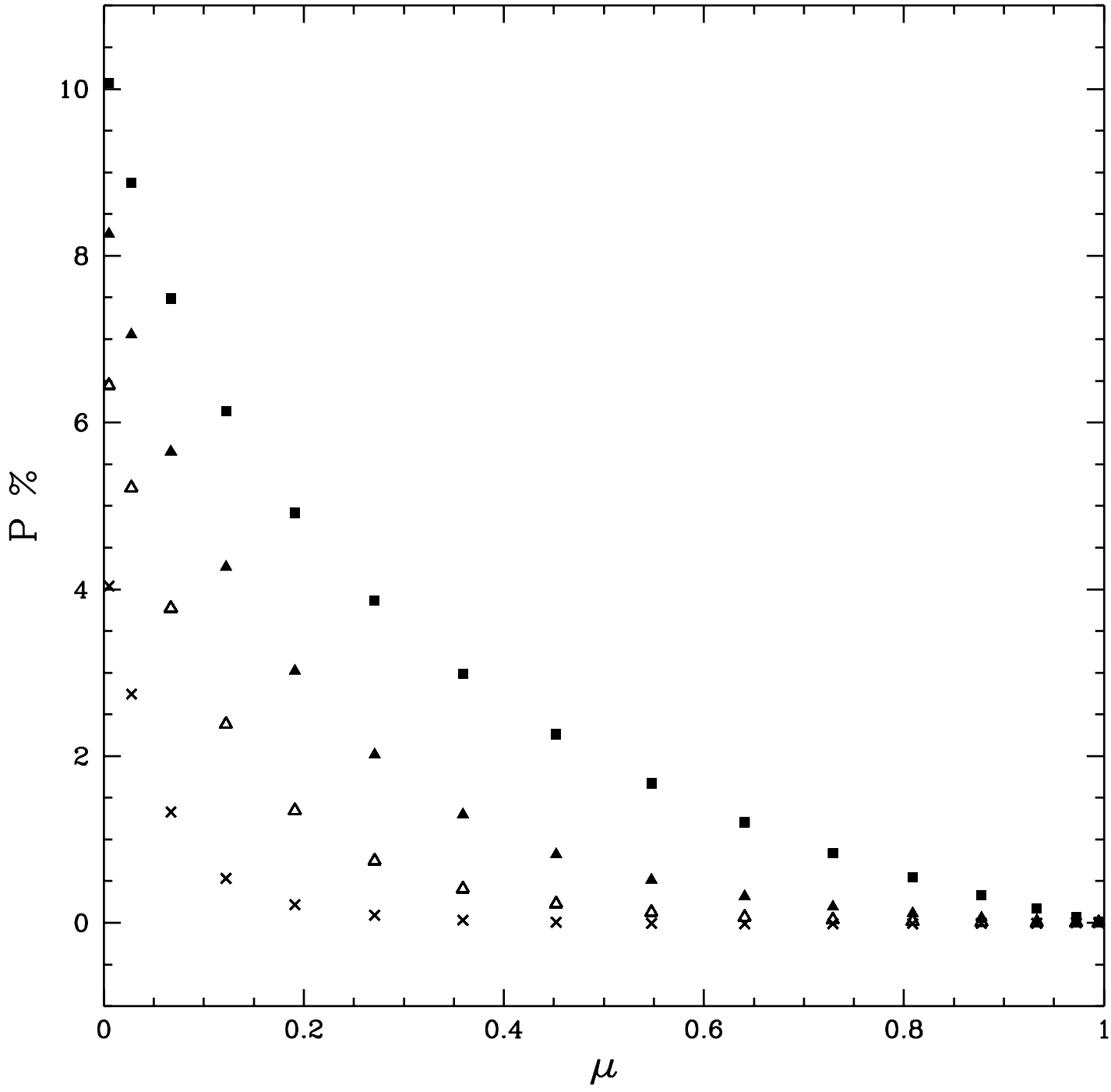
P %
10
8
6
4
2
0
0
0.2
0.4
0.6
0.8
1
μ

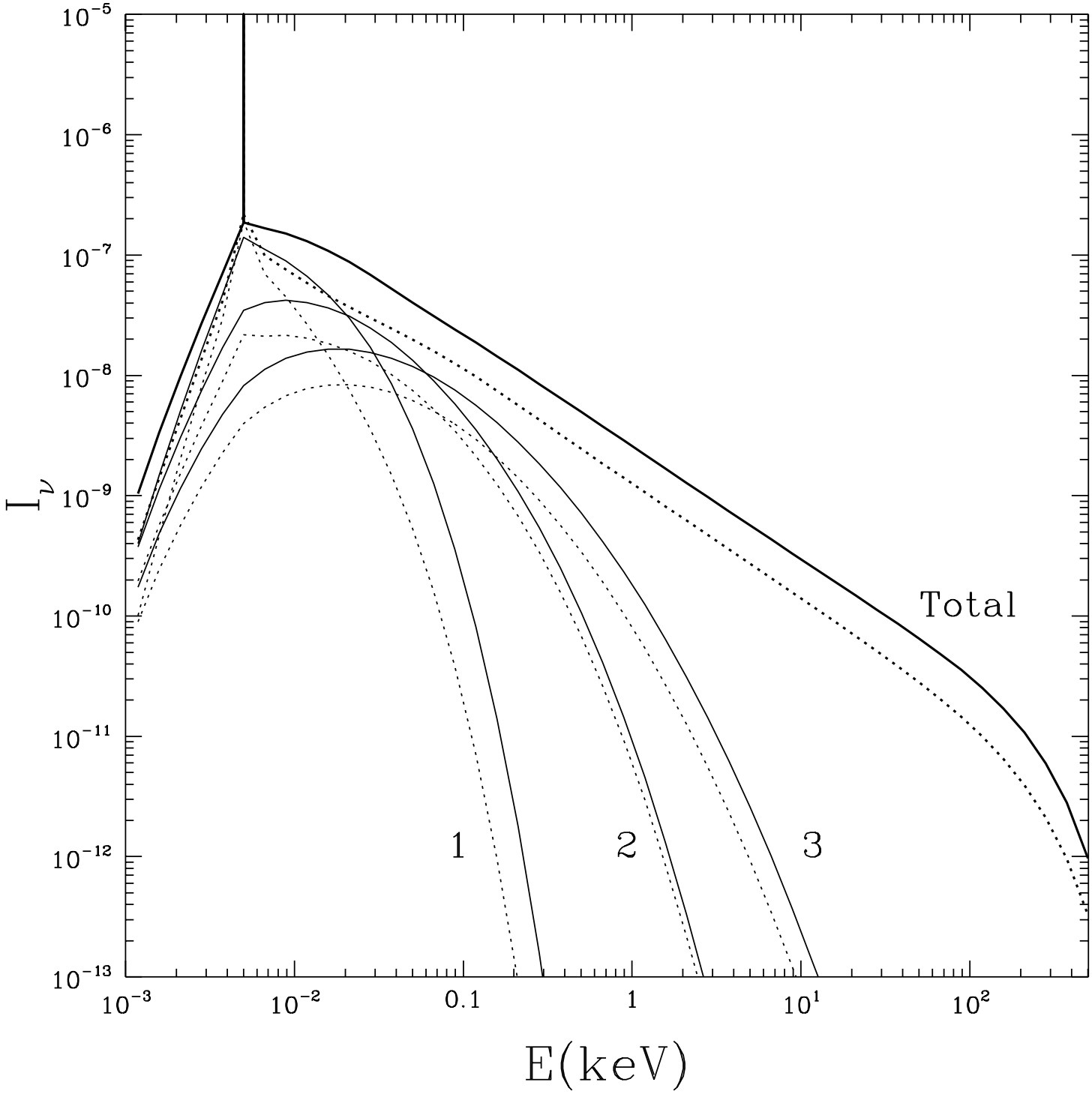
$10^{-5}$
$10^{-6}$
$10^{-7}$
$10^{-8}$
$10^{-9}$
$10^{-10}$
$10^{-11}$
$10^{-12}$
$10^{-13}$
$I_\nu$
$10^{-3}$
$10^{-2}$
0.1
1
$10^{1}$
$10^{2}$
E(keV)
Total
1
2
3

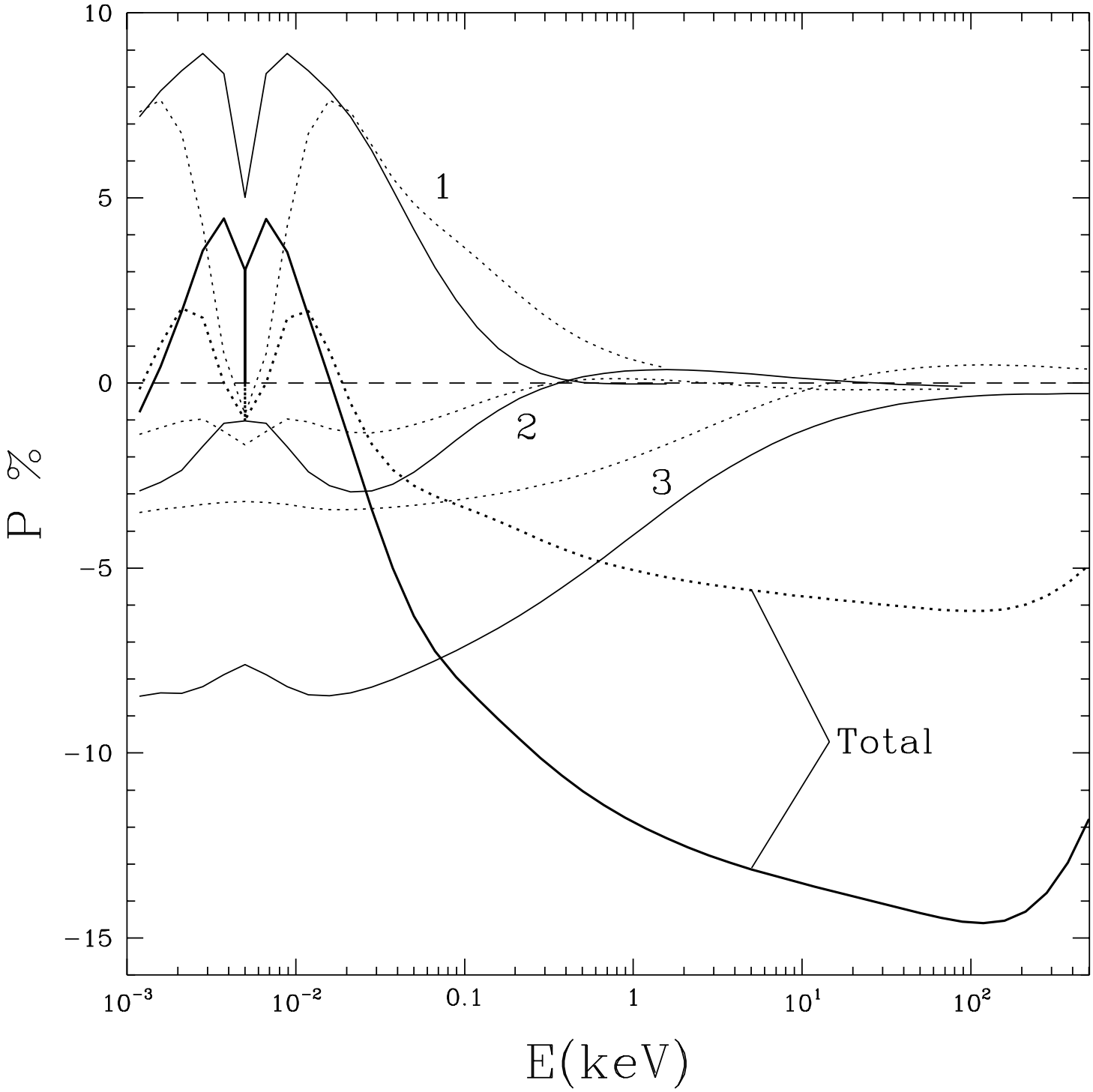
10
5
0
−5
−10
−15
P %
1
2
3
Total
$10^{-3}$
$10^{-2}$
0.1
1
$10^{1}$
$10^{2}$
E(keV)

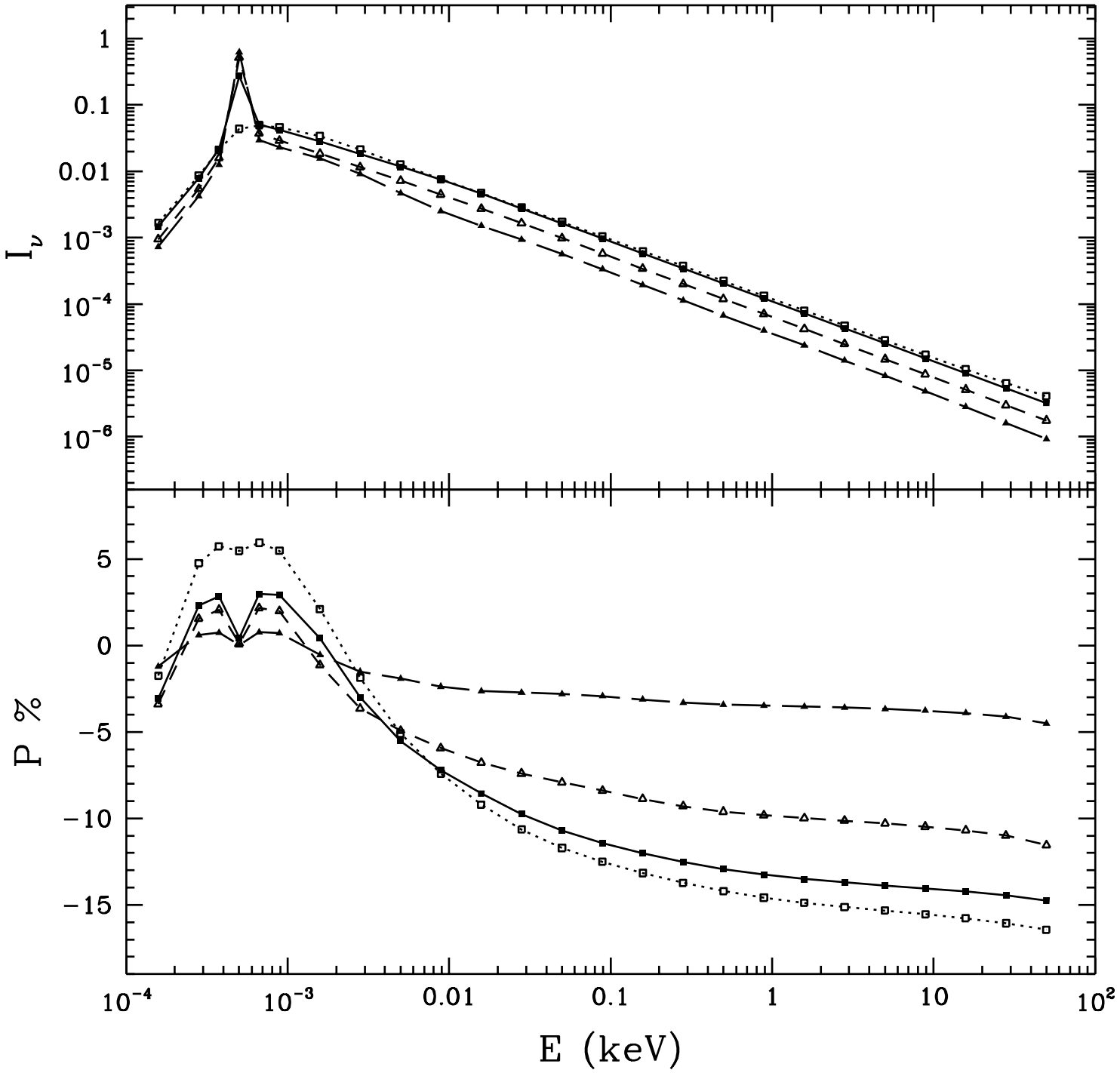
1
0.1
0.01
$10^{-3}$
$10^{-4}$
$10^{-5}$
$10^{-6}$
$I_\nu$
5
0
−5
−10
−15
P %
$10^{-4}$
$10^{-3}$
0.01
0.1
1
10
$10^{2}$
E (keV)

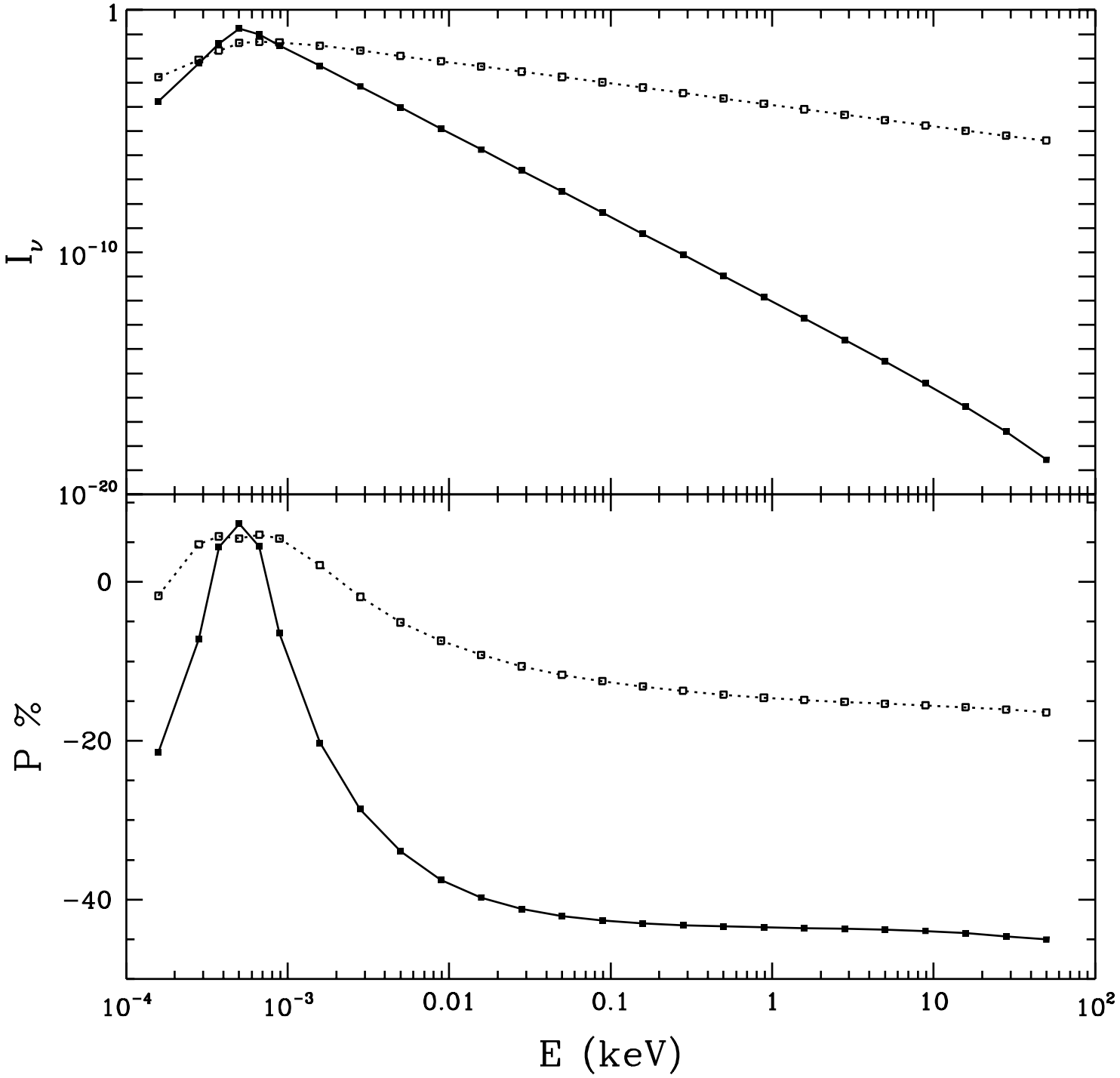
1
$10^{-10}$
$10^{-20}$
$I_\nu$
0
−20
−40
P %
$10^{-4}$
$10^{-3}$
0.01
0.1
1
10
$10^{2}$
E (keV)

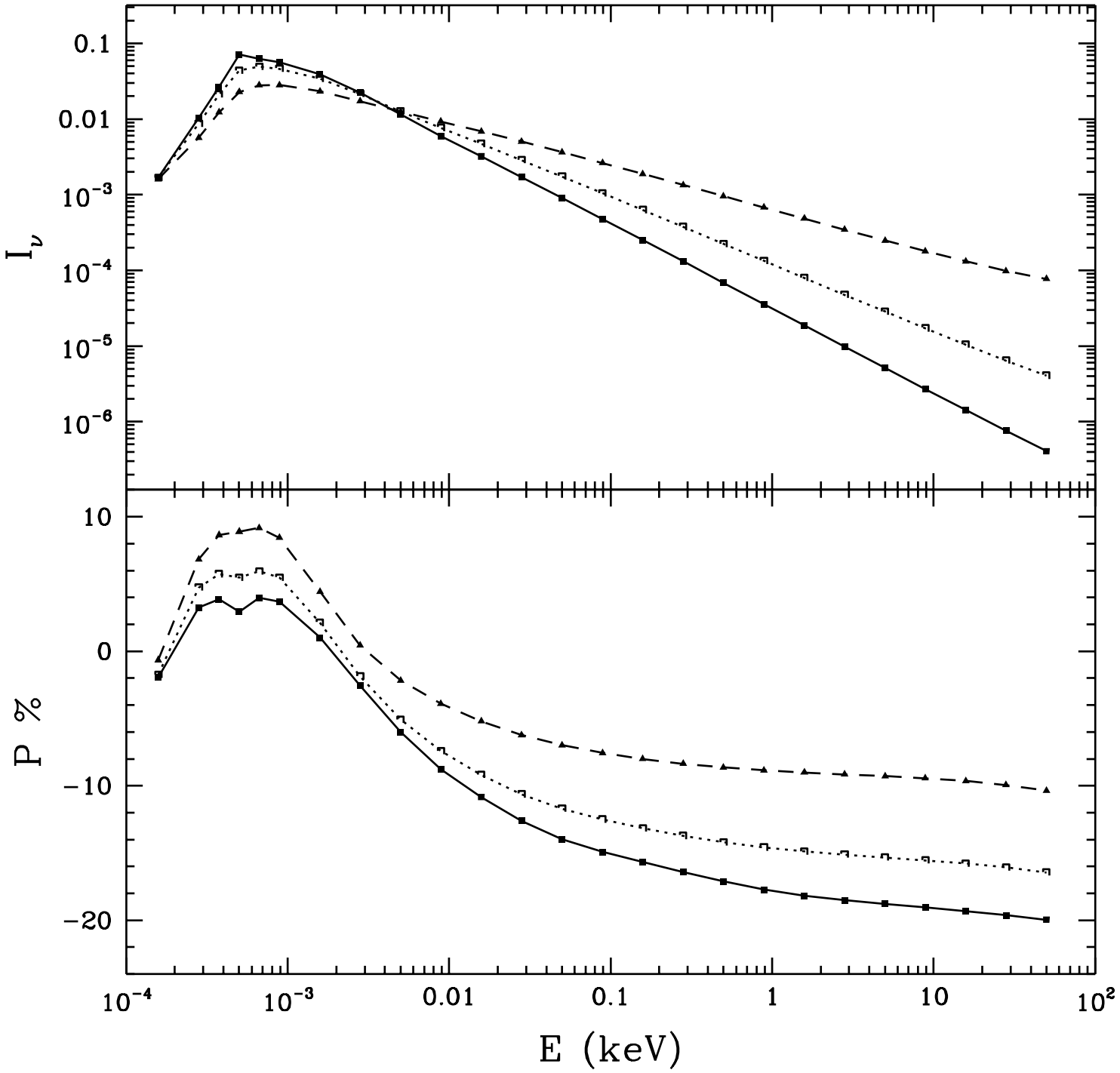
0.1
0.01
$10^{-3}$
$10^{-4}$
$10^{-5}$
$10^{-6}$
$I_\nu$
10
0
−10
−20
P %
$10^{-4}$
$10^{-3}$
0.01
0.1
1
10
$10^{2}$
E (keV)

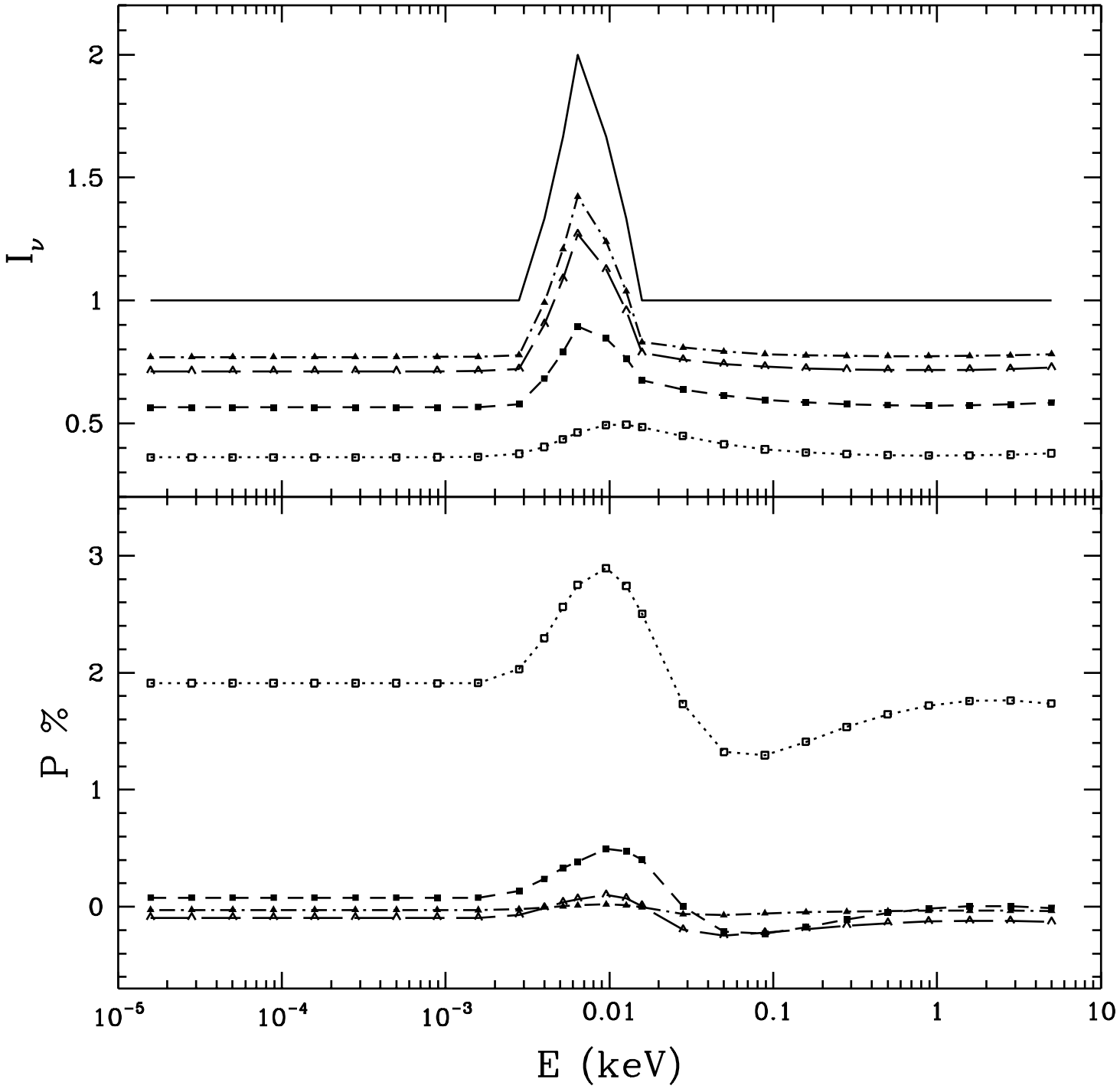
2
1.5
1
0.5
$I_\nu$
3
2
1
0
P %
$10^{-5}$
$10^{-4}$
$10^{-3}$
0.01
0.1
1
10
E (keV)

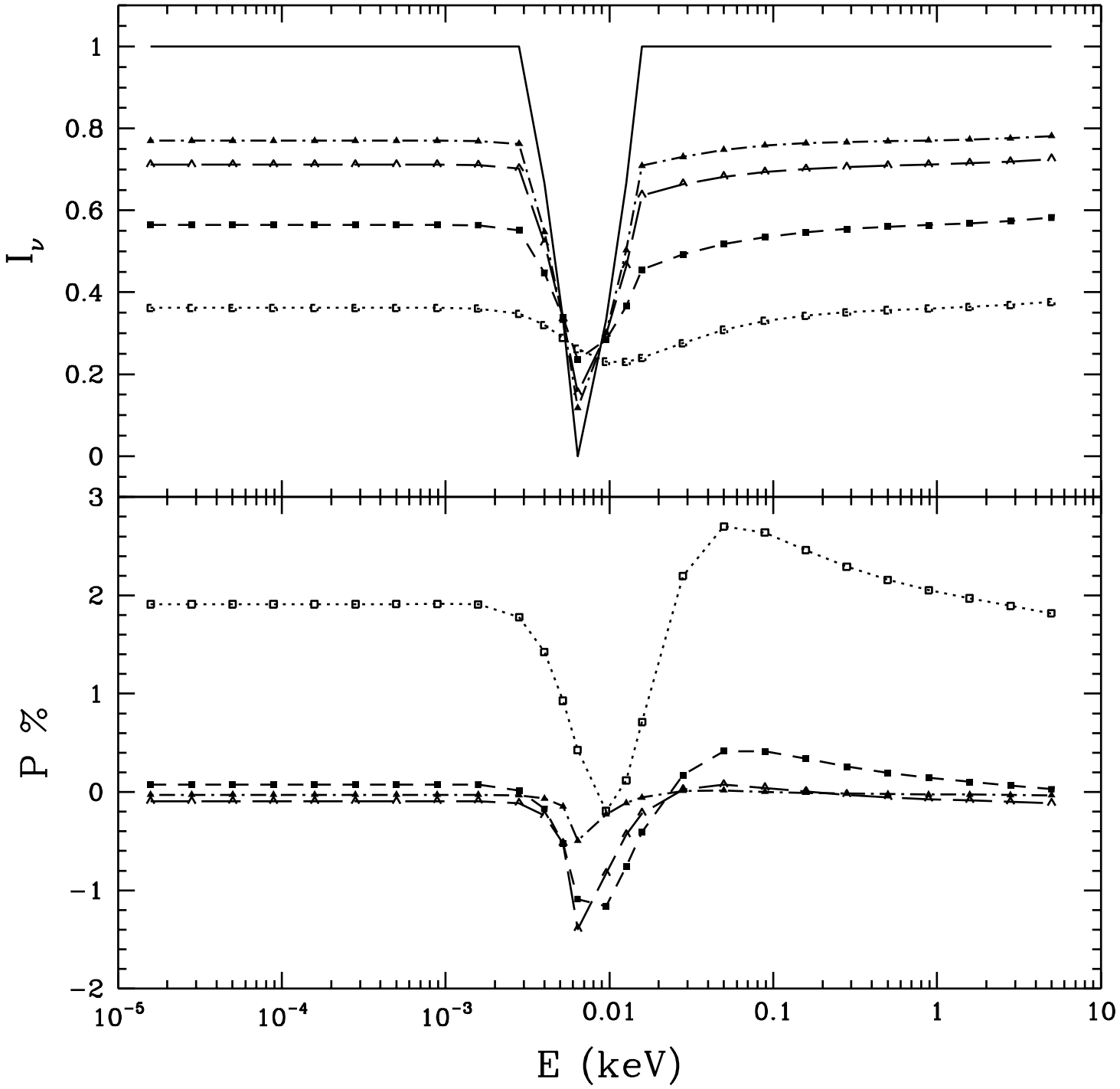
1
0.8
0.6
0.4
0.2
0
$I_\nu$
3
2
1
0
−1
−2
P %
$10^{-5}$
$10^{-4}$
$10^{-3}$
0.01
0.1
1
10
E (keV)

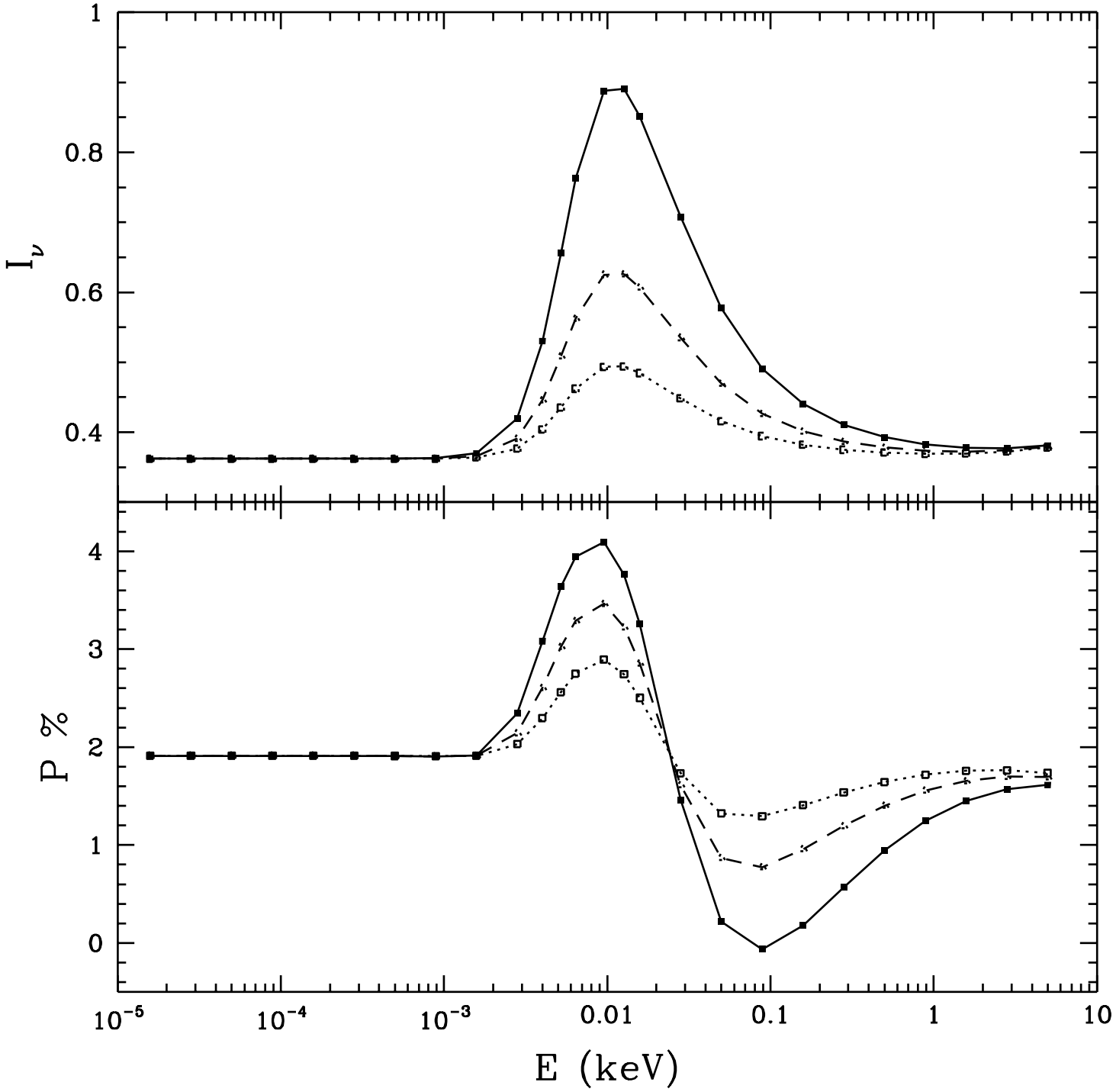
1
0.8
0.6
0.4
$I_\nu$
4
3
2
1
0
P %
$10^{-5}$
$10^{-4}$
$10^{-3}$
0.01
0.1
1
10
E (keV)

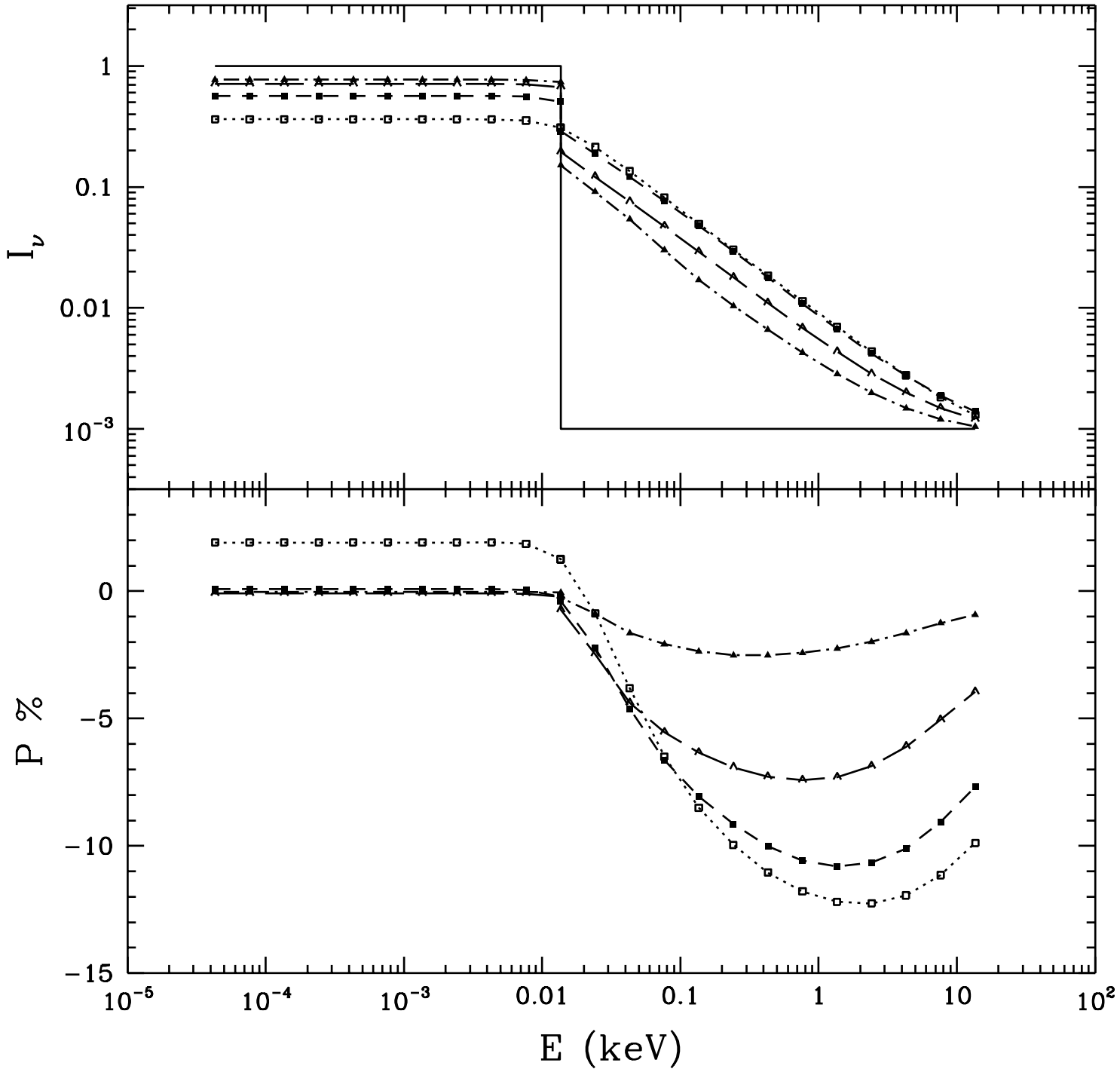
1
0.1
0.01
$10^{-3}$
$I_\nu$
0
−5
−10
−15
P %
$10^{-5}$
$10^{-4}$
$10^{-3}$
0.01
0.1
1
10
$10^2$
E (keV)

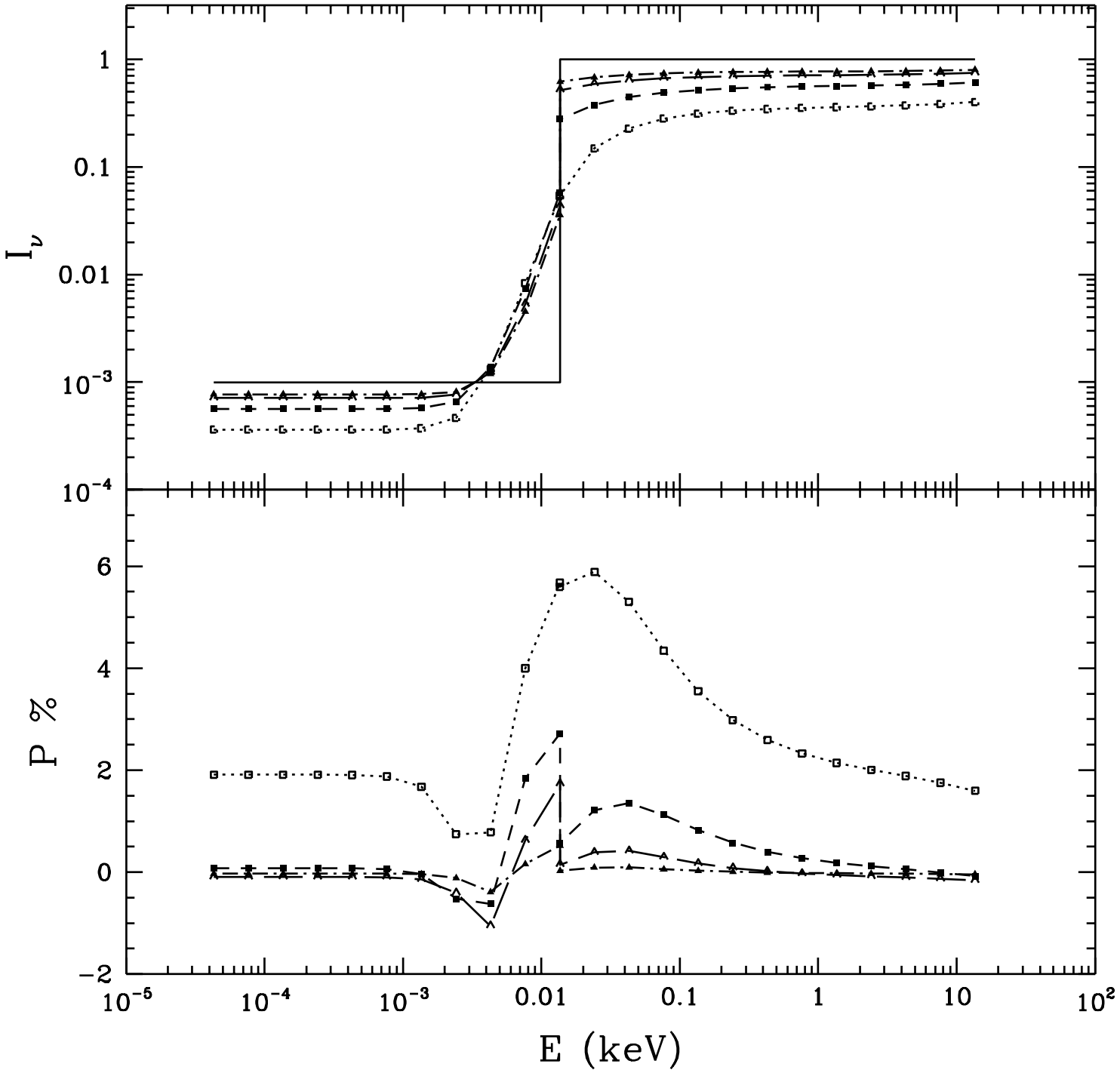
1
0.1
0.01
$10^{-3}$
$10^{-4}$
$I_\nu$
6
4
2
0
−2
P %
$10^{-5}$
$10^{-4}$
$10^{-3}$
0.01
0.1
1
10
$10^2$
E (keV)

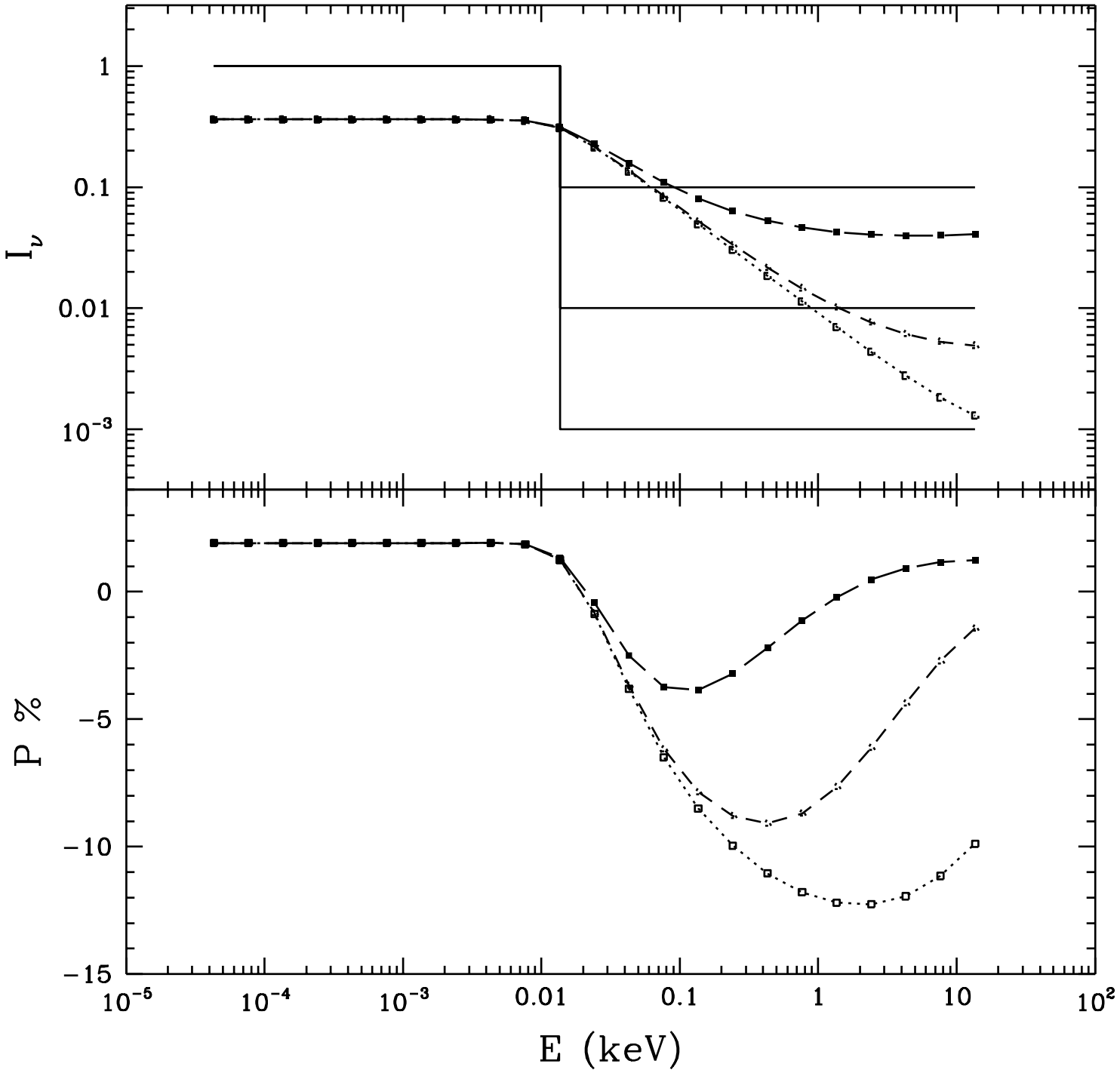
1
0.1
0.01
$10^{-3}$
$I_\nu$
0
−5
−10
−15
P %
$10^{-5}$
$10^{-4}$
$10^{-3}$
0.01
0.1
1
10
$10^2$
E (keV)

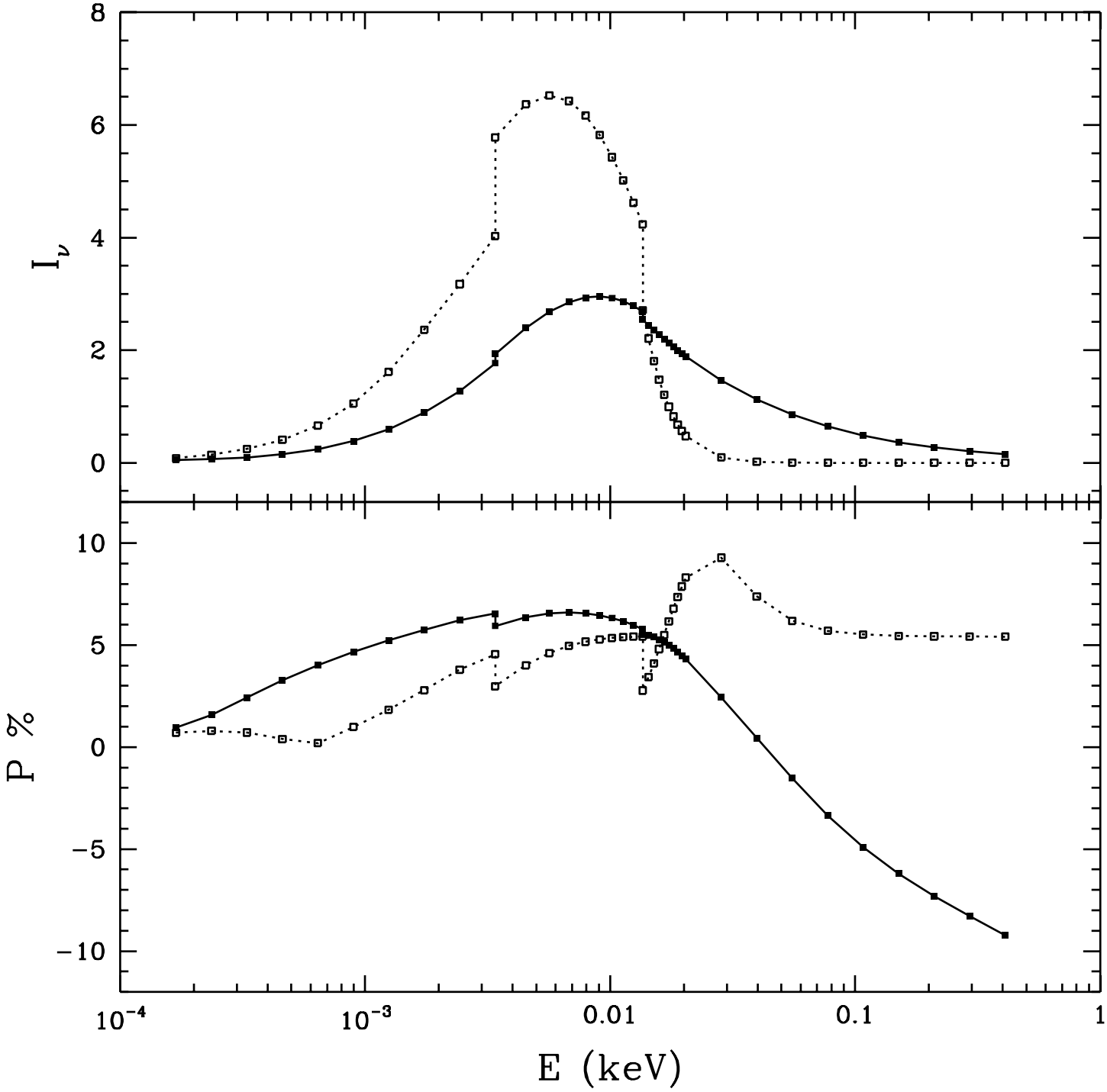
8
6
4
2
0
$I_\nu$
10
5
0
−5
−10
P %
$10^{-4}$
$10^{-3}$
0.01
0.1
1
E (keV)

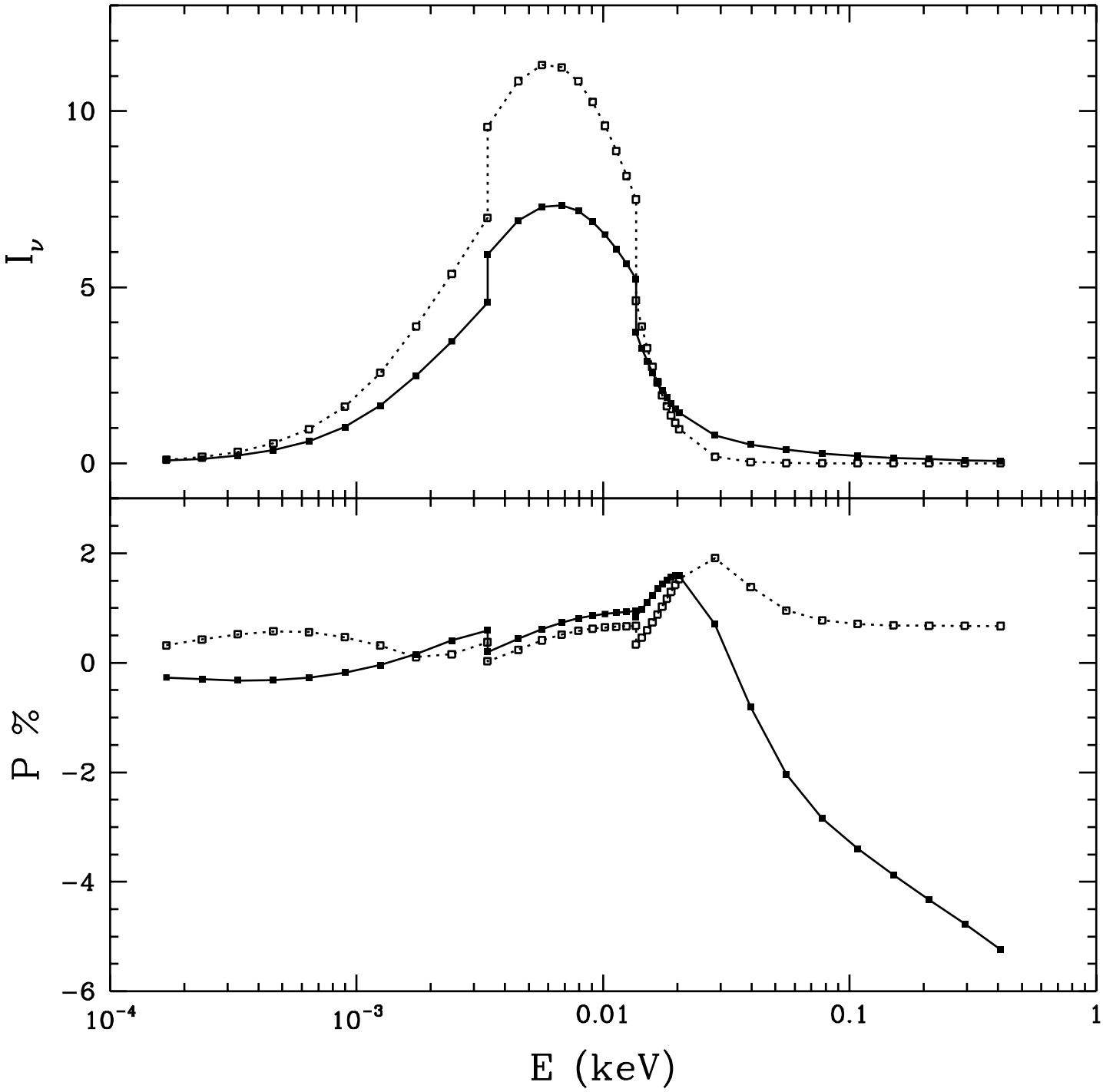
10
5
0
$I_\nu$
2
0
−2
−4
−6
P %
$10^{-4}$
$10^{-3}$
0.01
0.1
1
E (keV)